

Euclid Quick Data Release (Q1)

Extending the quest for little red dots to $z < 4$

Euclid Collaboration: L. Bisigello^{*1}, G. Rodighiero^{2,1}, S. Fotopoulou³, F. Ricci^{4,5}, K. Jahnke⁶, A. Feltre⁷, V. Allevalo⁸, F. Shankar⁹, P. Cassata^{2,1}, E. Dalla Bontà^{2,1,10}, G. Gandolfi^{11,1}, G. Girardi^{2,1}, M. Giuliatti¹², A. Grazian¹, C. C. Lovell¹³, R. Maiolino¹⁴, T. Matamoros Zatarain³, M. Mezcua^{15,16}, I. Prandoni¹², D. Roberts⁹, W. Roster¹⁷, M. Salvato¹⁷, M. Siudek^{18,15}, F. Tarsitano¹⁹, Y. Toba^{20,21,22}, A. Vietri², L. Wang^{23,24}, G. Zamorani²⁵, M. Baes²⁶, S. Belladitta^{6,25}, A. Nersesian^{27,26}, L. Spinoglio²⁸, X. Lopez Lopez^{29,25}, N. Aghanim³⁰, B. Altieri³¹, A. Amara³², S. Andreon³³, N. Auricchio²⁵, H. Aussel³⁴, C. Baccigalupi^{35,36,37,38}, M. Baldi^{39,25,40}, A. Balestra¹, S. Bardelli²⁵, A. Basset⁴¹, P. Battaglia²⁵, R. Bender^{17,42}, A. Biviano^{36,35}, A. Bonchi⁴³, E. Branchini^{44,45,33}, M. Brescia^{46,8}, J. Brinchmann^{47,48}, S. Camera^{49,50,51}, G. Cañas-Herrera^{52,53,54}, V. Capobianco⁵¹, C. Carbone⁵⁵, J. Carretero^{56,57}, S. Casas⁵⁸, M. Castellano⁵, G. Castignani²⁵, S. Cavuoti^{8,59}, K. C. Chambers⁶⁰, A. Cimatti⁶¹, C. Colodro-Conde⁶², G. Congedo⁶³, C. J. Conselice⁶⁴, L. Conversi^{65,31}, Y. Copin⁶⁶, F. Courbin^{67,68}, H. M. Courtois⁶⁹, M. Cropper⁷⁰, A. Da Silva^{71,72}, H. Degaudenzi¹⁹, G. De Lucia³⁶, A. M. Di Giorgio²⁸, C. Dolding⁷⁰, H. Dole³⁰, F. Dubath¹⁹, C. A. J. Duncan⁶⁴, X. Dupac³¹, S. Dusini⁷³, A. Ealet⁶⁶, S. Escoffier⁷⁴, M. Farina²⁸, R. Farinelli²⁵, F. Faustini^{43,5}, S. Ferriol⁶⁶, F. Finelli^{25,75}, M. Frailis³⁶, E. Franceschi²⁵, S. Galeotta³⁶, K. George⁴², W. Gillard⁷⁴, B. Gillis⁶³, C. Giocoli^{25,40}, P. Gómez-Alvarez^{76,31}, J. Gracia-Carpio¹⁷, B. R. Granett³³, F. Grupp^{17,42}, S. Gwyn⁷⁷, S. V. H. Haugan⁷⁸, H. Hoekstra⁵⁴, W. Holmes⁷⁹, I. M. Hook⁸⁰, F. Hormuth⁸¹, A. Hornstrup^{82,83}, P. Hudelot⁸⁴, M. Jhabvala⁸⁵, E. Keihänen⁸⁶, S. Kermiche⁷⁴, A. Kiessling⁷⁹, B. Kubik⁶⁶, M. Kümmel⁴², M. Kunz⁸⁷, H. Kurki-Suonio^{88,89}, Q. Le Boulc'h⁹⁰, A. M. C. Le Brun⁹¹, D. Le Mignant⁹², P. Liebing⁷⁰, S. Ligorì⁵¹, P. B. Lilje⁷⁸, V. Lindholm^{88,89}, I. Lloro⁹³, G. Mainetti⁹⁰, D. Maino^{94,55,95}, E. Maiorano²⁵, O. Mansutti³⁶, S. Marcin⁹⁶, O. Marggraf⁹⁷, M. Martinelli^{5,98}, N. Martinet⁹², F. Marulli^{29,25,40}, R. Massey⁹⁹, S. Maurogordato¹⁰⁰, E. Medinaceli²⁵, S. Mei^{101,102}, M. Melchior¹⁰³, Y. Mellier^{104,84}, M. Meneghetti^{25,40}, E. Merlin⁵, G. Meylan¹⁰⁵, A. Mora¹⁰⁶, M. Moresco^{29,25}, L. Moscardini^{29,25,40}, R. Nakajima⁹⁷, C. Neissner^{107,57}, S.-M. Niemi⁵², J. W. Nightingale¹⁰⁸, C. Padilla¹⁰⁷, S. Paltani¹⁹, F. Pasian³⁶, K. Pedersen¹⁰⁹, W. J. Percival^{110,111,112}, V. Pettorino⁵², S. Pires³⁴, G. Polenta⁴³, M. Poncet⁴¹, L. A. Popa¹¹³, L. Pozzetti²⁵, F. Raison¹⁷, R. Rebolo^{114,115,62}, A. Renzi^{2,73}, J. Rhodes⁷⁹, G. Riccio⁸, E. Romelli³⁶, M. Roncarelli²⁵, E. Rossetti³⁹, H. J. A. Rottgering⁵⁴, B. Rusholme¹¹⁶, R. Saglia^{42,17}, Z. Sakr^{117,118,119}, D. Sapone¹²⁰, B. Sartoris^{42,36}, J. A. Schewtschenko⁶³, M. Schirmer⁶, P. Schneider⁹⁷, T. Schrabback¹²¹, M. Scodreggio⁵⁵, A. Secroun⁷⁴, G. Seidel⁶, S. Serrano^{16,122,15}, P. Simon⁹⁷, C. Sirignano^{2,73}, G. Sirri⁴⁰, L. Stanco⁷³, J. Steinwagner¹⁷, P. Tallada-Crespí^{56,57}, A. N. Taylor⁶³, H. I. Teplitz¹²³, I. Tereno^{71,124}, S. Toft^{125,126}, R. Toledo-Moreo¹²⁷, F. Torradeflot^{57,56}, I. Tutusaus¹¹⁸, L. Valenziano^{25,75}, J. Valiviita^{88,89}, T. Vassallo^{42,36}, G. Verdoes Kleijn²⁴, A. Veropalumbo^{33,45,44}, Y. Wang¹²³, J. Weller^{42,17}, A. Zacchei^{36,35}, F. M. Zerbi³³, I. A. Zinchenko⁴², E. Zucca²⁵, M. Ballardini^{128,129,25}, M. Bolzonella²⁵, E. Bozzo¹⁹, C. Burigana^{12,75}, R. Cabanac¹¹⁸, A. Cappi^{25,100}, D. Di Ferdinando⁴⁰, J. A. Escartin Vigo¹⁷, L. Gabarra¹³⁰, M. Huertas-Company^{62,18,131,132}, J. Martín-Fleitas¹⁰⁶, S. Matthew⁶³, M. Maturi^{117,133}, N. Mauri^{61,40}, A. Pezzotta¹⁷, M. Pöntinen⁸⁸, C. Porciani⁹⁷, I. Risso¹³⁴, V. Scottez^{104,135}, M. Sereno^{25,40}, M. Tenti⁴⁰, M. Viel^{35,36,38,37,136}, M. Wiesmann⁷⁸, Y. Akrami^{137,138}, I. T. Andika^{139,140}, S. Anselmi^{73,2,141}, M. Archidiacono^{94,95}, F. Atrio-Barandela¹⁴², C. Benoist¹⁰⁰, K. Benson⁷⁰, D. Bertacca^{2,1,73}, M. Bethermin¹⁴³, A. Blanchard¹¹⁸, L. Blot^{144,141}, M. L. Brown⁶⁴, S. Bruton¹⁴⁵, A. Calabro⁵, F. Caro⁵, C. S. Carvalho¹²⁴, T. Castro^{36,37,35,136}, Y. Charles⁹², F. Cogato^{29,25}, T. Contini¹¹⁸, A. R. Cooray¹⁴⁶, O. Cucciati²⁵, S. Davini⁴⁵, F. De Paolis^{147,148,149}, G. Desprez²⁴, A. Díaz-Sánchez¹⁵⁰, J. J. Diaz⁶², S. Di Domizio^{44,45}, J. M. Diego¹⁵¹, A. Enia^{39,25}, Y. Fang⁴², A. G. Ferrari⁴⁰, P. G. Ferreira¹³⁰, A. Finoguenov⁸⁸, A. Fontana⁵, F. Fontanot^{36,35}, A. Franco^{148,147,149}, K. Ganga¹⁰¹, J. García-Bellido¹³⁷, T. Gasparotto³⁶, V. Gautard¹⁵², E. Gaztanaga^{15,16,13}, F. Giacomini⁴⁰, F. Gianotti²⁵, G. Gozaliasl^{153,88}, M. Guidi^{39,25}, C. M. Gutierrez¹⁵⁴, A. Hall⁶³, W. G. Hartley¹⁹, S. Hemmati¹¹⁶, C. Hernández-Monteagudo^{115,62}, H. Hildebrandt¹⁵⁵, J. Hjorth¹⁰⁹, J. J. E. Kajava^{156,157}, Y. Kang¹⁹, V. Kansal^{158,159}, D. Karagiannis^{128,160}, K. Kiiveri⁸⁶, C. C. Kirkpatrick⁸⁶, S. Kruk³¹, J. Le Graet⁷⁴, L. Legrand^{161,162}, M. Lembo^{128,129}, F. Lepori¹⁶³, G. Leroy^{164,99}, G. F. Lesci^{29,25}, J. Lesgourgues⁵⁸, L. Leuzzi^{29,25}, T. I. Liaudat¹⁶⁵, A. Loureiro^{166,167}, J. Macias-Perez¹⁶⁸, G. Maggio³⁶, M. Magliocchetti²⁸, E. A. Magnier⁶⁰, C. Mancini⁵⁵, F. Mannucci⁷, R. Maoli^{169,5}, C. J. A. P. Martins^{170,47}, L. Maurin³⁰, M. Miluzio^{31,171}, P. Monaco^{172,36,37,35}, C. Moretti^{38,136,36,35,37}, G. Morgante²⁵, S. Nadathur¹³, K. Naidoo¹³, A. Navarro-Alsina⁹⁷,

S. Nesseris¹³⁷, F. Passalacqua^{2, 73}, K. Paterson⁶, L. Patrizii⁴⁰, A. Pisani^{74, 173}, D. Potter¹⁶³, S. Quai^{29, 25}, M. Radovich¹, P.-F. Rocci³⁰, S. Sacquegna^{147, 148, 149}, M. Sahlén¹⁷⁴, D. B. Sanders⁶⁰, E. Sarpa^{38, 136, 37}, C. Scarlata¹⁷⁵, J. Schaye⁵⁴, A. Schneider¹⁶³, D. Sciotti^{5, 98}, E. Sellentin^{176, 54}, A. Shulevski^{177, 24, 54, 178}, L. C. Smith¹⁷⁹, K. Tanidis¹³⁰, C. Tao⁷⁴, G. Testera⁴⁵, R. Teyssier¹⁷³, S. Tosi^{44, 134}, A. Troja^{2, 73}, M. Tucci¹⁹, C. Valieri⁴⁰, A. Venhola¹⁸⁰, D. Vergani²⁵, G. Verza¹⁸¹, P. Vielzeuf⁷⁴, A. Viitanen^{86, 5}, N. A. Walton¹⁷⁹, J. R. Weaver¹⁸², E. Soubrie³⁰, and D. Scott¹⁸³

(Affiliations can be found after the references)

Received ; accepted

ABSTRACT

Recent *James Webb* Space Telescope (JWST) observations have revealed an interesting population of sources with a compact morphology and a characteristic ‘v-shaped’ continuum, namely blue at rest-frame $\lambda < 4000 \text{ \AA}$ and red at longer wavelengths. The nature of these sources, called ‘little red dots’ (LRDs), is still highly debated, since it is unclear if they host active galactic nuclei (AGN) and their number seems to drastically drop at $z < 4$. We take advantage of the 63 deg^2 covered by the quick *Euclid* Quick Data Release (Q1) to extend the search for LRDs to brighter magnitudes and to lower redshifts than what has been possible with JWST. This is fundamental to have a broader view of the evolution of this peculiar galaxy population. The selection is performed by fitting the available photometric data (*Euclid*, the *Spitzer* Infrared Array Camera (IRAC), and ground-based *griz* data) with two power laws, to retrieve both the rest-frame optical and UV slopes consistently over a large redshift range (i.e. $z < 7.6$). We then exclude extended objects and possible line emitters, and perform a careful visual inspection to remove any imaging artefacts. The final selection includes 3341 LRD candidates from $z = 0.33$ to $z = 3.6$, with 29 detected also in IRAC. The resulting rest-frame UV luminosity function, in contrast with previous JWST studies, shows that the number density of LRD candidates increases from high-redshift down to $z = 1.5$ – 2.5 and decreases at even lower redshifts. However, less evolution is apparent focusing on the subsample of more robust LRD candidates having also IRAC detections, which however is affected by low statistics and limited by the IRAC resolution. The comparison with previous quasar (QSO) UV luminosity functions shows that LRDs are not the dominant AGN population at $z < 4$ and $M_{\text{UV}} < -21$. Follow-up studies of these LRD candidates are pivotal to confirm their nature, probe their physical properties and check for their compatibility with JWST sources, given that the different spatial resolution and wavelength coverage of *Euclid* and JWST could select different samples of compact sources.

Key words. Galaxies: active - Galaxies: luminosity function - Galaxies: evolution

1. Introduction

Supermassive black holes (SMBHs) of tens of millions of Solar masses appear to be ubiquitous at the centres of local galaxies (e.g., Magorrian et al. 1998; Gültekin et al. 2009). Moreover, a close co-evolution linking SMBHs to their host galaxies is suggested by tight scaling relations observed between the SMBH masses and different galactic properties (e.g., Magorrian et al. 1998; Silk & Rees 1998; Gebhardt et al. 2000; Ferrarese 2002; Mullaney et al. 2012; Delvecchio et al. 2022). However, theoretical models calibrated against present-day scaling relations seem to produce a wide range of SMBH properties at higher redshifts, due to differences in the implementation of supernova and BH feedback and sub-grid physics (e.g., Habouzit et al. 2020, 2021). It is therefore important to extend the analysis of SMBHs and their host galaxies to a wide range of times.

Observational evidence for massive accreting BHs shining as AGN at increasingly higher redshifts puts strong constraints on their formation scenarios and the mass of their seeds. Indeed, forming a $10^9 M_{\odot}$ SMBH by $z = 7$ requires either a heavy seed ($M_{\text{BH}} \sim 10^5 M_{\odot}$), a light seed ($M_{\text{BH}} \sim 10^2 M_{\odot}$) accreting for some time at super-Eddington or hyper-Eddington rates (e.g., Wyithe & Loeb 2012; Alexander & Natarajan 2014; Inayoshi et al. 2016; Begelman & Volonteri 2017; Pacucci et al. 2017; Pacucci & Loeb 2022; Maiolino et al. 2024c), or primordial BHs formed as a result of fluctuations in the early Universe (Hawking 1971; Carr & Hawking 1974; Dayal et al. 2024). It is, however, unclear if the currently observed high- z AGN can be considered representative of the whole AGN population. The study of low-luminosity AGN and low-mass SMBHs is therefore key to placing constraints on the mass distribution for seeds of high- z AGN.

The epoch of reionisation marks the transition phase at which the first sources of ultraviolet (UV) radiation were able, after the

so-called ‘Dark Ages’, to ionise hydrogen atoms in the surrounding intergalactic medium for the first time (Barkana & Loeb 2001; Dayal & Ferrara 2018). However, it is still largely debated which sources were responsible for this process. Many studies identify low-mass metal-poor star-forming galaxies at high redshift as the main driver of cosmic reionisation (e.g., Atek et al. 2024; Simmonds et al. 2024; Dayal 2024), while others show evidence that faint AGN can contribute significantly to reionisation (e.g., Asthana et al. 2024), and in some cases dominate reionisation (e.g., Madau et al. 2024; Grazian et al. 2024). Quantifying the number density of such faint AGN is therefore fundamental to constrain their contribution to reionising the Universe.

The first years of observations with JWST have revealed a new intriguing population of compact red sources characterised by a peculiar ‘v-shaped’ spectral energy distribution (SED), namely a blue rest-frame UV continuum and a steep red slope in the rest-frame optical (e.g., Kocevski et al. 2023, 2024; Harikane et al. 2023; Matthee et al. 2024; Greene et al. 2024; Labbé et al. 2023; Labbe et al. 2023; Killi et al. 2024; Furtak et al. 2023). These so-called ‘little red dots’ (LRDs), mainly observed at $z \geq 4$, can be easily selected by photometric observations, given their compact morphology and peculiar SED shape. However, particular care needs to be taken to remove contaminating populations, like brown dwarfs that correspond to 21% of colour-selected JWST LRD candidates, following Langeroodi & Hjorth (2023).

The nature of these LRDs is heavily debated. Indeed, their steep rest-frame optical slopes are consistent with either a reddened AGN continuum or emission from dusty star formation (e.g., Kocevski et al. 2023; Barro et al. 2023; Labbé et al. 2023; Akins et al. 2024), with evidence supporting both scenarios. For example, spectroscopic follow-up studies of LRDs have shown that around 80% of them show broad hydrogen ($H\alpha$ and $H\beta$) emission (e.g., Kocevski et al. 2023, 2024; Kokorev

* e-mail: laura.bisigello@inaf.it

et al. 2024a; Killi et al. 2024; Matthee et al. 2024; Furtak et al. 2023; Greene et al. 2024; Wang et al. 2024), with line widths of generally $\text{FWHM} \leq 1000 \text{ km s}^{-1}$, but with some going as up as 3000 km s^{-1} . These line widths would far exceed that of typical star-forming galaxies at lower redshift (e.g., Fumagalli et al. 2012), supporting the AGN scenario. In this picture, we have a direct view of the broad-line region and the accretion disk of the AGN, but with foreground dust attenuation originating either from a dusty interstellar medium (ISM) or from nuclear dust (see, e.g., Netzer 2015; Hickox & Alexander 2018). This scenario would make LRDs similar to the ‘red quasars’ observed at lower redshifts (e.g., Webster et al. 1995; Richards et al. 2003; Urrutia et al. 2008; Glikman et al. 2012, 2015), considering also that some of these red quasar show a similar excess of UV light (Wethers et al. 2018; Stepney et al. 2024). While the majority of LRDs may host an AGN, they represent a sub-sample of the overall AGN population. Indeed, out of the large number of broad line AGN discovered by JWST, only 10–30% have SEDs typical of LRDs (Hainline et al. 2024).

The SMBH masses inferred for these LRDs lie in the range $M_{\text{BH}} = 10^6\text{--}10^8 M_{\odot}$, while their stellar masses range from 10^7 to $10^{11} M_{\odot}$, showing that a fraction of them are over-massive relative to their host galaxies’ stellar masses when compared to the local $M_{\text{BH}}\text{--}M_{\star}$ relation (e.g., Maiolino et al. 2024b; Harikane et al. 2023), while they are consistent with the local relation between M_{BH} and stellar velocity dispersion (Maiolino et al. 2024b). This finding indicates they may be going through super-Eddington accretion or originate from heavy BH seeds. Bellovary (2025) has instead recently hypothesised that LRDs could be runaway-collapse globular clusters with tidal disruption events, which could explain their compact size, UV luminosities, and large number densities.

In the scenario where LRDs are totally powered by dusty starbursts, they would correspond to very massive galaxies ($M_{\star} = 10^9\text{--}10^{11} M_{\odot}$). However, in this picture, we would end up with an excess of massive early galaxies, some of which in tension with cosmological models and some so compact to be unstable against supernovae feedback (Wang et al. 2024; Akins et al. 2024), supporting the AGN scenario. However, mid-infrared (mid-IR) observations at 5–25 μm have shown a remarkably flat continuum, favouring SED models consistent with a dusty, compact starburst and only a mild contribution from an obscured AGN (Williams et al. 2024; Pérez-González et al. 2024) or an AGN torus deficient of hot dust (Barro et al. 2024). Up to now, only two LRDs have been detected in the far-IR, providing some indications of warm dust emission (Barro et al. 2024; Juodžbalis et al. 2024). Moreover, several broad-line objects show a clear Balmer break in their spectra, implying that evolved stars may indeed contribute to the rest-frame optical (Kokorev et al. 2024b), though the precise contribution is highly degenerate (Wang et al. 2024).

In addition, the majority of LRDs are not strong X-ray emitters, being undetected (or marginally detected) even in very deep observations or using stacking analysis (Ananna et al. 2024; Yue et al. 2024). For this reason, some studies have hypothesised that the broad-line components could not be due to an AGN, but to outflows driven by star formation or inelastic Raman scattering of stellar UV continua by neutral hydrogen atoms (Kokubo & Harikane 2024). Alternatively, some studies have reported that the broadening could be consistent with the stellar velocity dispersion, if the galaxy is going through a short-lived phase when the central densities are much higher than at later times (Baggen et al. 2024). Other studies have instead suggested that the X-ray weakness could be due to a very steep X-ray spectrum, in-

duced by the absorption by large, Compton thick columns, or a very high BH accretion rate (Maiolino et al. 2024a). The last two scenarios would also explain the non-detection at radio frequencies (Mazzolari et al. 2024). The presence of dense neutral gas around the AGN accretion disc would also mimic a Balmer break, indicating that the rest-frame optical may not be due to evolved stars (Inayoshi & Maiolino 2024). However, the absence of variability in the rest-frame UV, except for a few LRDs (Zhang et al. 2024), may point against a strong contribution by AGN (Tee et al. 2024; Kokubo & Harikane 2024).

The uncertainties on the nature of the LRDs are, at least partially, driven by their high- z nature, which implies they are faint and require near-IR observations. While preliminary studies trying to find low- z and local analogues have been performed by, for example, Noboriguchi et al. (2023), Mezcua et al. (2024), and Lin et al. (2024), large near-IR surveys are necessary to follow the redshift evolution of LRDs, since their number density has been suggested to dramatically drop at $z < 4$ (Kocevski et al. 2024). Moreover, such large near-IR surveys are key to probe their clustering on large scales with Tanaka et al. (2024) already suggesting that LRDs may show an excess of clustering at kpc scales. The large area observed and the near-IR coverage of *Euclid* (Euclid Collaboration: Mellier et al. 2024) is therefore ideal to search and study LRDs.

In this work we search for LRDs using the newly available *Euclid* Quick Release Q1 (2025), combined with publicly available *Spitzer* Infrared Array Camera (IRAC) images and ground-based optical data. The area and depth of these *Euclid* observations are ideal to have a first characterisation of the bright end of the LRD luminosity function and to extend the search to $z < 4$. To select LRDs, we follow the approach by Kocevski et al. (2024) and select them using cuts on the rest-frame optical and UV slopes. The paper is structured as follows. In Sect. 2 we present a summary of the *Euclid* data products used in this work, as well as the ancillary IRAC images. In Sect. 3 we outline our selection method and discuss our findings in Sect. 4. The final conclusion and future prospects are reported in Sect. 5. Throughout the paper, we consider a ΛCDM cosmology with $H_0 = 70 \text{ km s}^{-1} \text{ Mpc}^{-1}$, $\Omega_{\text{m}} = 0.27$, $\Omega_{\Lambda} = 0.73$. All magnitudes are reported in the AB system (Oke & Gunn 1983).

2. Data description

2.1. *Euclid* data products

An overview of the Q1 data release is described in Euclid Collaboration: Aussel et al. (2025), the Visible Camera (VIS) and Near-Infrared Spectrometer and Photometer (NISP) processing and data products are in Euclid Collaboration: McCracken et al. (2025) and Euclid Collaboration: Polenta et al. (2025), respectively, while the photometric catalogue is discussed in Euclid Collaboration: Romelli et al. (2025). An overview of the *Euclid* ESA mission’s scientific objectives is reported in Euclid Collaboration: Mellier et al. (2024).

Briefly, Q1 includes 63 deg^2 of the extragalactic sky, divided into three fields: 22 deg^2 in the Euclid Deep Field North (EDF-N); 12 deg^2 in the Euclid Deep Field Fornax (EDF-F); and 28 deg^2 in the Euclid Deep Field South (EDF-S). Each field has been observed in four photometric bands, one in the visible (I_{E} , Euclid Collaboration: Cropper et al. 2024), and three in the near-IR (NISP, Y_{E} , J_{E} , and H_{E} band, see Euclid Collaboration: Jahnke et al. 2024). In addition, these observations are complemented with ground-based observations carried out with multiple instruments covering between $0.3 \mu\text{m}$ and $0.9 \mu\text{m}$, as part of the Ultra-

Table 1. The filters used in this work, with associated observed depths.

Band	λ_{eff} [μm]	EDF-F	EDF-N	EDF-S
CFHT/MegaCam <i>u</i>	0.372		23.4	
HSC <i>g</i>	0.480		24.9	
CFHT/MegaCam <i>r</i>	0.640		24.0	
PAN-STARRS <i>i</i>	0.755		23.1	
HSC <i>z</i>	0.891		23.3	
Decam <i>g</i>	0.473	24.6		24.7
Decam <i>r</i>	0.642	24.3		24.4
Decam <i>i</i>	0.784	23.8		23.8
Decam <i>z</i>	0.926	23.1		23.1
VIS/ I_E	0.715	24.7	24.7	24.7
NISP/ Y_E	1.085	23.1	23.2	23.1
NISP/ J_E	1.375	23.2	23.3	23.3
NISP/ H_E	1.773	23.2	23.2	23.2
IRAC/IRAC1	3.550	24.0	24.0	23.1
IRAC/IRAC2	4.493	24.0	24.0	23.0
IRAC/IRAC3	5.696	21.2	20.0	
IRAC/IRAC4	7.799	19.9	21.1	

Notes. Reported magnitudes are the 10σ observed depths. Optical and *Euclid* magnitudes refer to an extended source in a $2 \times \text{FWHM}$ diameter aperture and correspond to the median depths of the observing tiles (Euclid Collaboration: Romelli et al. 2025). For IRAC1 and IRAC2 values see Euclid Collaboration: Moneti et al. (2022) and Euclid Collaboration: McPartland et al. (2024), depths correspond to average values in the fields derived considering $2''$ empty apertures. For the IRAC3 and IRAC channels we report the average depths derived from the catalogue, after correcting from aperture to total magnitudes.

Table 2. Area coverage in deg^2 of the available IRAC images (Euclid Collaboration: Moneti et al. 2022).

Channel	EDF-F	EDF-N	EDF-S
IRAC1	10.52	11.74	23.60
IRAC2	11.05	11.54	23.14
IRAC3	7.78	0.61	...
IRAC4	7.77	0.62	...

violet Near-Infrared Optical Northern Survey (UNIONS, Gwyn et al. in prep.) or the Dark Energy Survey (Abbott et al. 2018). The complete list of filters available in each field and their corresponding observational depths are reported in Table 1.

In this work we consider aperture photometry measured for all bands on the images convolved to the worst spatial resolution (usually a ground based band). We consider an aperture with a diameter of 2 full width at half maximum (FWHM, median value of $1''.3$) and we correct it to total (see Euclid Collaboration: Romelli et al. 2025, for more details). We also correct each flux for galactic extinction, using the relation by Gordon et al. (2023) and the position of each source.

2.2. IRAC photometry

We start from the collection of IRAC images described in Euclid Collaboration: Moneti et al. (2022) covering a fraction of the Euclid Deep Fields (EDFs) as part of the Cosmic Dawn survey (Euclid Collaboration: McPartland et al. 2024). The images result from a collection of different programmes with non-uniform coverage, both in area and depth. We report the average 10σ depths in Table 1 and the area coverage in Table 2. The IRAC3

and IRAC4 filters are available only for a small portion of the EDF-F and EDF-N, while they are not available for the EDF-S.

Starting from the public images, we remove the sky background using the PHOTUTILS python package (Bradley et al. 2023), deriving the median value using a $3 \text{ pixel} \times 3 \text{ pixel}$ filter. Using the same package, we then use the position of all *Euclid* sources to extract aperture photometry with $1''$ radius aperture, consistent with half the worst FWHM of IRAC, on all available IRAC images. In this preliminary work, no attempt is made to de-blend IRAC sources using *Euclid* positions. For this reason a careful visual check is performed when selecting LRD candidates to remove objects affected by blending.

To derive the correction from aperture to total fluxes for all four IRAC filters, we compare this catalogue with a separate extraction, performed only for the EDF-N (Bisigello et al. in prep.). The extraction is performed using as detection image the co-added IRAC1 and IRAC2 images, weighted for each uncertainty map, and considering Kron apertures, derived with a scaling parameter of the unscaled Kron radius of 1.8 and a minimum value for the unscaled Kron radius of 2.5 pixels. We then match the two EDF-N catalogues, with aperture and Kron fluxes, to derive the aperture-to-total correction in each filter. We apply the same correction in all three fields.

We verify that the total fluxes are consistent with the catalogues described in Euclid Collaboration: Zalesky et al. (2024), which, however, cover only two out of three EDFs and include only the IRAC1 and IRAC2 filters. The comparison is shown in Appendix A, showing that magnitudes derived in this work are on average brighter by 0.1 magnitudes in the EDF-F and by 0.3 magnitudes in the EDF-N, with respect to the magnitudes presented in the Cosmic Dawn Catalogue. The agreement is, however, within 0.1 magnitudes if we consider only bright objects (i.e., IRAC1 or IRAC2 < 21).

2.3. Photometric redshifts

As a first estimate of the photometric redshift, we consider the median value and the two first modes derived in the main *Euclid* pipeline, which are described in detail in Euclid Collaboration: Tucci et al. (2025). In addition, given that these estimates are limited to $z = 6$, we consider also the redshift estimation derived for NISP-detected objects extending the redshift range up to $z = 12$. In this case we consider the redshift of the first peak of the probability distribution as the best estimate. As tested in Appendix B, the redshift estimation for LRDs derived from the pipeline includes about 40% of outliers, because LRD templates are not included in the pipeline at the moment. We will discuss later the method we use to improve over these estimates.

3. Sample selection

Previous JWST photometric studies have identified LRDs mainly by applying some colour cuts to compact sources (e.g., Barro et al. 2023; Labbe et al. 2023; Kokorev et al. 2024a). However, this type of selection is difficult to apply directly to *Euclid*, given the different filter set. In addition, a simple colour cut does not allow to have a selection of sources uniform across different redshifts, given that it is based on observed and not rest-frame properties. Therefore, we consider the alternative approach adopted by Kocovski et al. (2024) and select sources with compact morphology, red continuum in the rest-frame optical wavelengths, and blue continuum in the the rest-frame UV. The latter two quantities are directly derived by fitting the available

Table 3. Number of sources retrieved by different steps of the LRD selection in the three EDFs.

	EDF-F	EDF-N	EDF-S
Total sources	5 328 489	11 378 352	13 060 965
Reliable objects	3 640 908	7 342 804	8 588 063
IRAC-detected, $z \leq 6$	2 762 173	2 556 970	4 388 869
$N_{\text{filter}, S/N > 3} \geq 4$	1 094 377 (43%)	631 576 (23%)	1 850 820 (43%)
v-shaped continuum	891 (0.08%)	616 (0.09%)	3848 (0.2%)
Compact	42 (5%)	22 (4%)	173 (5%)
No emission lines	20 (48%)	8 (36%)	86 (50%)
$\chi^2 < 100$	16 (80%)	7 (87%)	82 (94%)
Visual inspection	8 (50%)	1 (14%)	20 (24%)
No-IRAC, $z \leq 2.1$	1 021 175	4 520 496	3 935 178
$N_{\text{filter}, S/N > 3} \geq 4$	189 275 (18%)	692 437 (15%)	735 675 (19%)
v-shaped continuum	15 838 (8%)	45 797 (7%)	59 035 (8%)
Compact	624 (4%)	1611 (3%)	2804 (5%)
No emission lines	558 (90%)	1344 (83%)	2560 (91%)
$\chi^2 < 100$	546 (87%)	1233 (76%)	2509 (98%)
Visual inspection	422 (77%)	970 (79%)	1920 (76%)
Total $z > 6$ candidates	24 050	71 776	53 131
Reliable galaxies	12 325 (51%)	27 535 (38%)	42 564 (80%)
IRAC-detected	3508 (28%)	5024 (18%)	4534 (11%)
$N_{\text{filter}, S/N > 3} \geq 4$	1883 (54%)	3098 (62%)	1617 (36%)
v-shaped continuum	103 (5%)	128 (4%)	68 (4%)
Compact	0	0	0

Notes. For the definition of the different selections we refer to Sect. 3. Percentages correspond to the percentage of objects selected in one line with respect to the line above.

photometric data. Below we report in details the entire classification procedure we apply, while in Table 3 we report the original numbers of sources in each field and how they change at different selection steps.

3.1. LRD selection procedure

As a first conservative selection, we remove objects classified as stars (PHZ_CLASSIFICATION = 1) using the classification from the PHZ processing function (Euclid Collaboration: Tucci et al. 2025). It is important to notice that this classification is based on photometry and not on compactness, which is fundamental to not remove any LRD candidates. We also retrieve from the *Euclid* archive only galaxies with reliable photometry, defined as having DET_QUALITY_FLAG = 0, SPURIOUS_FLAG = 0, and FLAG = 0 for any *Euclid* filter. This selection allows us to remove objects in the proximity of bright stars, blended sources, saturated or bad pixels, and sources contaminated by close neighbours. We refer to the subsample of objects obtained after this selection step as reliable objects.

We proceed by removing objects outside the area covered by IRAC observations, as these bands are fundamental to extending the search of LRDs at $z > 2$. For the same reason we keep only objects with signal-to-noise $S/N > 3$ in the IRAC1 or IRAC2 filter. We refer to these objects as IRAC-detected sources. Moreover, to fit at the same time both the UV and the optical rest-frame continuum we considered only objects with $S/N > 3$ in more than four filters. We also assure that there are at least two filters tracing the rest-frame UV continuum and two filters tracing the rest-frame optical one.

We continue by selecting only sources with the characteristic v-shaped continuum, following, as mentioned before, the approach by Kocevski et al. (2024). In particular, the continuum

slope β , defined such that $f_\lambda \propto \lambda^\beta$, is determined by performing a χ^2 minimisation fit to the observed magnitudes

$$m_i = -2.5 (\beta + 2) \log_{10} \left(\frac{\lambda_i}{\lambda_{\text{break}}} \right) + c, \quad (1)$$

where m_i is the AB magnitude measured in the i th filter with an effective wavelength of λ_i and $\lambda_{\text{break}} = 3645 \text{ \AA}$ is the wavelength of the break of the v-shape continuum. This fit is performed to derive both the rest-frame UV and optical spectral slopes, β_{UV} and β_{opt} . In Fig. 1, we report the filters used to fit β_{UV} and β_{opt} at different redshifts, considering both *Euclid*, ground-based bands, and the IRAC1 and IRAC2 IRAC filters. Given the filters availability and considering the small area coverage by the two longest IRAC filters, the fit is mainly possible between $z = 1$ and $z = 7.6$, for the EDF-F and EDF-S, while it can be extended down to $z = 0.6$ in the EDF-N, thanks to the presence of u -band observations. Considering that the redshifts of LRDs are not correctly recovered by the standard *Euclid* pipeline (see Appendix B), since at the moment LRD templates are not included, we include the redshift as a free parameter in the fit. We consider the median redshift from the pipeline as an initial guess and the first and second mode (i.e., first and second peak in the redshift probability distribution) redshifts as limits. For candidates at $z > 6$, the photometric redshift is derived considering a secondary branch of the pipeline, therefore in this case we consider the first peak of the redshift probability distribution as the initial guess. The fit is performed with the *Scipy* package (Virtanen et al. 2020). To take into account possible unknown uncertainties, we add in quadrature to the flux uncertainties 5% of the flux. In the fit we consider all available filters, but we include fluxes with $S/N < 3$ as 0 with an error equal to two times flux uncertainties, to take into account unknown uncertainties. Uncertainties on the output properties are derived repeating the fit

100 times after randomising the fluxes, considering a Gaussian function centred on the measured value and with σ equal to the flux uncertainties. The performance of the new redshift estimation and the redshift of the pipeline are analysed in [Appendix B](#).

Following the selection done by [Kocevski et al. \(2024\)](#), we select objects with

$$\begin{cases} \beta_{\text{opt}} > 0, \\ \beta_{\text{UV}} < -0.37, \\ \beta_{\text{UV}} > -2.8. \end{cases} \quad (2)$$

The third cut to the UV slope is applied to remove contamination by brown dwarfs. These objects have near-IR colours similar to reddened AGN, but they appear significantly bluer at shorter wavelengths ([Langeroodi & Hjorth 2023](#)). In addition, to assure a v-shape SED, when the two longest wavelength filters have $S/N > 3$, we request that the flux of the filter at the longest wavelength is the highest.

In order to select only compact sources, we consider sources with $\mu_{\text{max}} - m_{\text{point-like}} < -2.6$ mag arcsec⁻², which corresponds to the difference between the peak surface brightness above the background in the detection band (μ_{max}) and the expected magnitude for point-like sources ($m_{\text{point-like}}$). The chosen threshold has been optimised in the *Euclid* pipeline to select compact objects, like stars.

Given that a red rest-frame optical continuum can be mimicked by the presence of strong nebular emission lines, we performed an additional selection to remove such objects. In particular, the H α + $[\text{N II}]$ complex is present in the Y_e filter at $z = 0.44$ – 0.85 , in the J_e filter at $z = 0.77$ – 1.39 , in the H_e filter at $z = 1.31$ – 2.09 , and in the IRAC1 filter at $z = 3.82$ – 4.99 . In these redshift intervals, we impose that the flux of the contaminated band is lower than the flux of the next redward filter. A negative slope would indeed indicate the presence of strong nebular emission lines, even if the overall optical slope is consistent with our LRD slope selection. We notice that many previous JWST samples do not perform this selection and indeed LRD optical colours may be boosted by nebular emission lines ([Hainline et al. 2024](#)). However, a more complex analysis, which we leave for future studies, is necessary to understand if the underlying continuum of these strong line emitters is any way consistent with LRD selection.

We then look at the distribution of the χ^2 and remove any object with $\chi^2 \geq 100$, with this threshold chosen looking at the overall distribution of χ^2 and on random selection of SED.

Finally, given that the number of sources is limited, we visually check the *Euclid* and IRAC cutouts of any remaining object, to remove cases affected by blending issues in the IRAC bands, any remaining artefacts, or sources extended in the NISP filters. Future work, performing a detailed deblending analysis, could improve over this step. Unfortunately, this selection removes potential close pairs, which some LRDs may be part of (e.g., [Tanaka et al. 2024](#) found three dual LRD candidates over 0.54 deg²).

We also consider the photometric redshift estimation derived for NISP-detected sources that extend the redshift boundary at $z > 6$. As for the previous sample, we select only reliable sources, using the flagging available in the catalogue, we impose a detection in the IRAC filters, a $S/N > 3$ in at least four bands, and we select only v-shaped and compact sources. The number of sources selected in the different steps are listed in [Table 3](#), but, in the end, we do not obtain any additional LRD candidates.

At $z = 1$ – 2.1 the search for LRDs can be performed without the IRAC filters, since the J_e and H_e filters cover the rest-frame

optical continuum (see [Fig. 1](#)). Therefore, we repeat the selections described above, limiting the analysis to objects with the pipeline redshift $z_{\text{pipeline}} < 3$, as a conservative cut, but removing any object detected in IRAC. As for the previous selection, we look for objects detected in at least four filters (two blueward and two redward λ_{break}), with a v-shaped continuum, compact, with no evident contamination from strong nebular emission lines, and with $\chi^2 < 100$. We visually inspect the *Euclid* cutouts of any remaining object to remove any left artefact or extended objects.

The final sample of LRD candidates includes 29 objects with IRAC detections, corresponding to a density of 0.8 deg⁻², and 3312 objects without IRAC and limited to $z \leq 2.1$, corresponding to a density of 57.3 deg⁻². The total sample includes 3341 LRD candidates. The number of LRD candidates needs to be considered conservative, given the uncertainties in the rest-frame UV and optical slopes outline in [Appendix C](#) and the conservative selection steps performed. The complete list of LRD candidates and their properties is reported in [Table D.1](#), while the cutouts and photometric fit of two LRDs are shown as examples in [Figs 2 and 3](#).

3.2. Differences between the IRAC detected and IRAC undetected LRD candidates.

The difference in density of LRD candidates with and without IRAC is probably driven by several factors. On one side, the number of LRD candidates with IRAC may be underestimated, because blending issues can affect IRAC fluxes, producing a boost in the contaminated band which results in a large χ^2 , and at the same time we perform a more strict visual check removing any possible blended source. Indeed, as visible in [Table 3](#), the fraction of sources removed by the χ^2 cut and the visual inspection is larger for IRAC-detected sources. To understand the importance of blending, we verified that around 15% of all reliable *Euclid* sources have a projected sources within $2''$ (equal to the worst IRAC FWHM) and 5% within $1''$. Given that there are hints of LRDs could have an excess of clustering at kpc scales ([Tanaka et al. 2024](#)), the effect of blending may be even more strong in LRDs than in the general galaxy population. In addition, the FWHM of IRAC is larger than the radius used for the photometry, so flux loss may effect the detection of sources.

On the other side, the number of LRD candidates selected without IRAC may be overestimated, as the H α + $[\text{N II}]$ complex is inside H_e filter at $z = 1.31$ – 2.09 and the presence of the IRAC bands can help to identify them. In addition, the larger wavelength coverage can simply improve the removal of any type of contaminants.

However, some differences may be intrinsic. Indeed, observations with the JWST mid-infrared instrument (MIRI) have shown that the red rest-frame continuum becomes a remarkably flat continuum, indicating a mild contribution from an obscured AGN ([Williams et al. 2024](#); [Pérez-González et al. 2024](#)) or an AGN torus deficient of hot dust ([Barro et al. 2024](#)). At $z < 2.8$ IRAC bands cover the same rest-frame wavelengths as MIRI at $z > 5$, tracing indeed in the flat part of the SED.

4. Results

4.1. Observed properties of the LRD candidates

In [Fig. 4](#) we report the magnitude distributions in the four *Euclid* filters, showing that they are similar for all three fields, with the EDF-N having a light excess at bright magnitudes with respect of

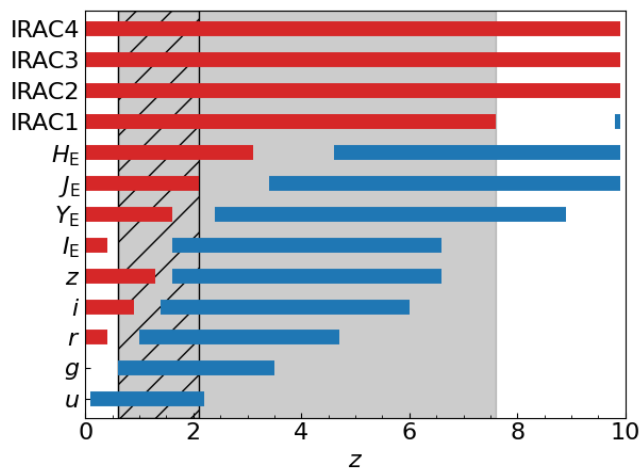


Fig. 1. Redshifts in which the different *Euclid*, IRAC, and ground-based filters trace the optical (red bars) or UV (blue bars) continuum. The grey shaded area indicates the redshift range in which we have at least four filters to derive the slopes necessary to select LRDs. The hatched area indicates the redshift range covered without IRAC.

the other two fields. Indeed, the mean magnitudes in the EDF-F and EDF-S differ by less than 0.1 mag, while the EDF-N shows slightly brighter magnitudes than the other two fields, anyway with a difference below 0.3 magnitudes. The similarities in the magnitude distributions of the three fields reassures us about the absence of strong biases or artefacts in one of them.

LRD candidates have mean magnitudes of $I_E = 25.5$, $Y_E = 24.3$, $J_E = 24.0$, and $H_E = 23.7$ and hence are relatively faint. Indeed, only 11% and 8% of them have magnitudes brighter than the 10σ depth in the H_E and I_E filters, respectively, while these fractions decrease to 7% and 3% in the J_E and Y_E filters. The sources detected in IRAC have a mean magnitudes of $IRAC1 = 22.2$ and $IRAC2 = 21.5$, showing that they are relatively bright in these two filters. In general, the fit is based only on four filters with $S/N > 3$ for 20% of the sample, while the remaining sources have from five to 10 filters with $S/N > 3$.

In Fig. 5 we report the photometric redshift distribution for the three fields. The average redshift is similar among the three fields and is $z = 1.7$. The average redshift of IRAC-detected LRD candidates is larger, that is $z = 2.4$, with no LRD candidates at $z \geq 4$.

4.2. Comparison with JWST LRD catalogues

In Fig. 6 we show a comparison of the redshift and M_{UV} at 1450 \AA of our sample of LRD candidates, derived by fitting the available data with two power laws, as explained in detail in Appendix B. We also compare our results with some of the previous samples derived with JWST data (Kocevski et al. 2024; Labbé et al. 2023; Kokorev et al. 2024a). Indeed, our sample is complementary to the JWST ones derived up to now, since it covers brighter magnitudes, with only one JWST source being as bright as the *Euclid* ones. It is also clear that our sample extends to lower redshifts than the JWST one. In the same figure we also show the M_{UV} that we expect to reach at the end of the *Euclid* mission. Indeed, the EDFs will be two magnitudes deeper when completed, which, even with IRAC data remaining unchanged, will allow us to reach $M_{UV} = -20$ at $z = 4$, extending the overlap with JWST, but also probing the bright end up to $z = 8$.

Table 4. FWHM of the *Euclid* VIS/NISP, JWST NIRCcam, and IRAC point spread functions.

Filter	FWHM		
	[arcsec]	[kpc] at $z = 1$	[kpc] at $z = 6$
<i>Euclid</i> / I_E	0.1	0.8	0.6
<i>Euclid</i> / H_E	0.3	2.5	1.8
JWST/F070W	0.029	0.2	0.17
JWST/F150W	0.050	0.4	0.29
JWST/F356W	0.116	0.96	0.67
JWST/F444W	0.145	1.19	0.85
IRAC/IRAC1	1.66–1.95 ^a	13.7–16.1	9.7–11.4
IRAC/IRAC2	1.72–2.02 ^a	14.2–16.6	10.0–11.8

Notes. Citations: *Euclid*/ I_E (Euclid Collaboration: McCracken et al. 2025), *Euclid*/ H_E (Euclid Collaboration: Polenta et al. 2025). JWST (Rigby et al. 2023). ^a The two numbers refer to when *Spitzer* was cryogenically cooled and when it was warm, respectively.

It is necessary, however, to consider that, even if we select only compact sources, the different angular resolution of JWST and *Euclid* could have an impact on the selection. In Table 4 we report the FWHM of the two missions at similar wavelengths, with the corresponding physical scales given at $z = 1$ and $z = 6$. The difference with respect to IRAC is even larger, reaching a factor of at least 10 in physical size. Therefore, follow-up campaigns will be necessary to confirm that the LRD candidates identified with *Euclid* and IRAC are as compact as the JWST ones.

4.3. Comparison with other *Euclid* AGN catalogues

The *Euclid* AGN catalogue presented by Euclid Collaboration: Matamoro Zatarain et al. (2025) focuses on the selection of AGN, mainly blue QSOs, based on *Euclid* photometry, but also ancillary data from UV to IR, as well as previous public spectroscopic data. Euclid Collaboration: Roster et al. (2025) instead did a careful matching of *Euclid* sources with public X-ray surveys, identifying X-ray detected AGN. We have therefore investigated how many of our LRD candidates are also present in these other catalogues of AGN candidates.

4.3.1. Optical photometric selections

The first selection they presented, named B24A, is based only on two *Euclid* colours and was presented in Euclid Collaboration: Bisigello et al. (2024). Taking into account the limitations of this colour selection, since it has both a low purity ($P = 0.166 \pm 0.015$) and a low completeness ($C = 0.347 \pm 0.004$), 254 (8%) of our LRD candidates could be classified as QSO candidates. The selection is indeed based on the $I_E - J_E$ and $I_E - Y_E$ colours, so it could trace the blue UV rest-frame slope, which is present in both LRDs and blue QSOs, but missing the red optical rest-frame slope.

The presence of observations in the u band in the EDF-N allows us to use an additional colour selection from Euclid Collaboration: Bisigello et al. (2024), applied again by Euclid Collaboration: Matamoro Zatarain et al. (2025). The selection, which we refer to as B24B, is based on the $u - z$ and $I_E - H_E$ colours, corresponding to a completeness of $C = 0.861 \pm 0.004$ and a purity $P = 0.992 \pm 0.017$. Of the entire sample of LRD candidates in the EDF-N, 258 (26%) are selected by the B24B selection.

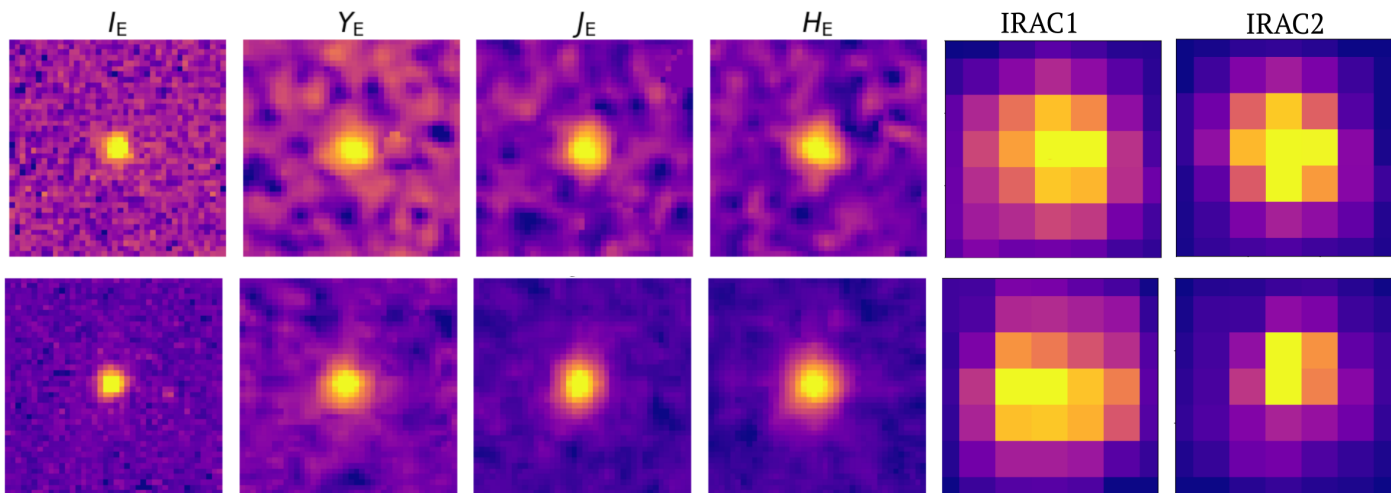


Fig. 2. Two example LRD candidates, showing $4'' \times 4''$ cutouts in the four *Euclid* filters and the two shortest IRAC channels. From left to right: I_E , Y_E , J_E , H_E , IRAC1, and IRAC2.

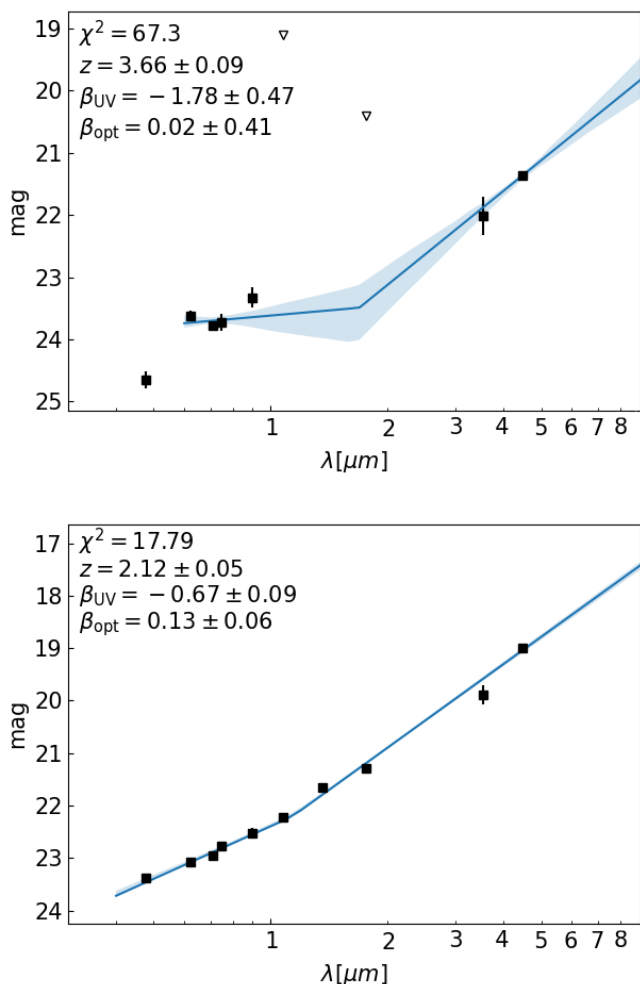


Fig. 3. Fit with two power-laws of the photometric data of the two example LRD candidates shown in Fig. 2. We show fluxes with $S/N > 3$ as black squares, while 3σ upper limits are shown with empty triangles. The best fit is shown with a blue solid line, while the shaded region shown the 16% and 84% uncertainties. We report on the top left the χ^2 and the output parameters.

In addition, [Euclid Collaboration: Matamoro Zatarain et al. \(2025\)](#) identified two new colour selections fine-tuned based on the colours occupied by DESI QSO. A first selection is based on *Euclid* colours ($I_E - Y_E$ and $J_E - H_E$) and a compactness criteria, while the second include also ground-based ancillary colours ($g - z$ and $I_E - H_E$). We refer to this selections as MZ25a and MZ25b, respectively. The first selection includes 1686 QSO candidates, corresponding to 50% of our catalogue, while the second criteria selects 1939 QSO candidates, corresponding to 58% of our catalogue.

The official *Euclid* catalogue ([Euclid Collaboration: Tucci et al. 2025](#)) includes also a probability of being a QSO, obtained by performing a supervised machine learning method called Probabilistic Random Forest (PRF, [Reis et al. 2019](#)), trained using photometric data only. Using this classification, [Euclid Collaboration: Matamoro Zatarain et al. \(2025\)](#) identified QSO as objects having a QSO probability above 85% and not being classified as stars. Of our sample, 34 (1%) LRD candidates are also classified as QSO using this method.

None of our LRD candidates are in the purified subsets of the *Gaia* QSO candidates catalogue (see Sect. 3.2.4. in [Euclid Collaboration: Matamoro Zatarain et al. 2025](#)) based on the Data Release 3 (DR3, [Gaia Collaboration: Vallenari et al. 2023](#)) or in the machine-learning classification based on *Euclid* images by [Euclid Collaboration: Margalef-Bentabol et al. \(2025\)](#).

4.3.2. Near-IR photometric selections

Taking advantage of the WISE coverage, [Euclid Collaboration: Matamoro Zatarain et al. \(2025\)](#) also applied the two photometric selections by [Assef et al. \(2018\)](#). With the selection corresponding to 75% completeness, called A18C75, 35 (1%) of the LRD galaxies are identified as potential QSOs. With the selection corresponding to 90% reliability, called A18R90, only four LRD candidates are also QSO candidates.

In addition, given that IRAC observations are available for at least part of the sample, we verify if any of our LRD candidates satisfy the AGN selection by [Donley et al. \(2012\)](#). Unfortunately, in the EDF-S this selection can not be applied, as there are observations only on two IRAC bands. In the other two fields, only two LRD candidates has a $S/N > 3$ in all four IRAC filters and

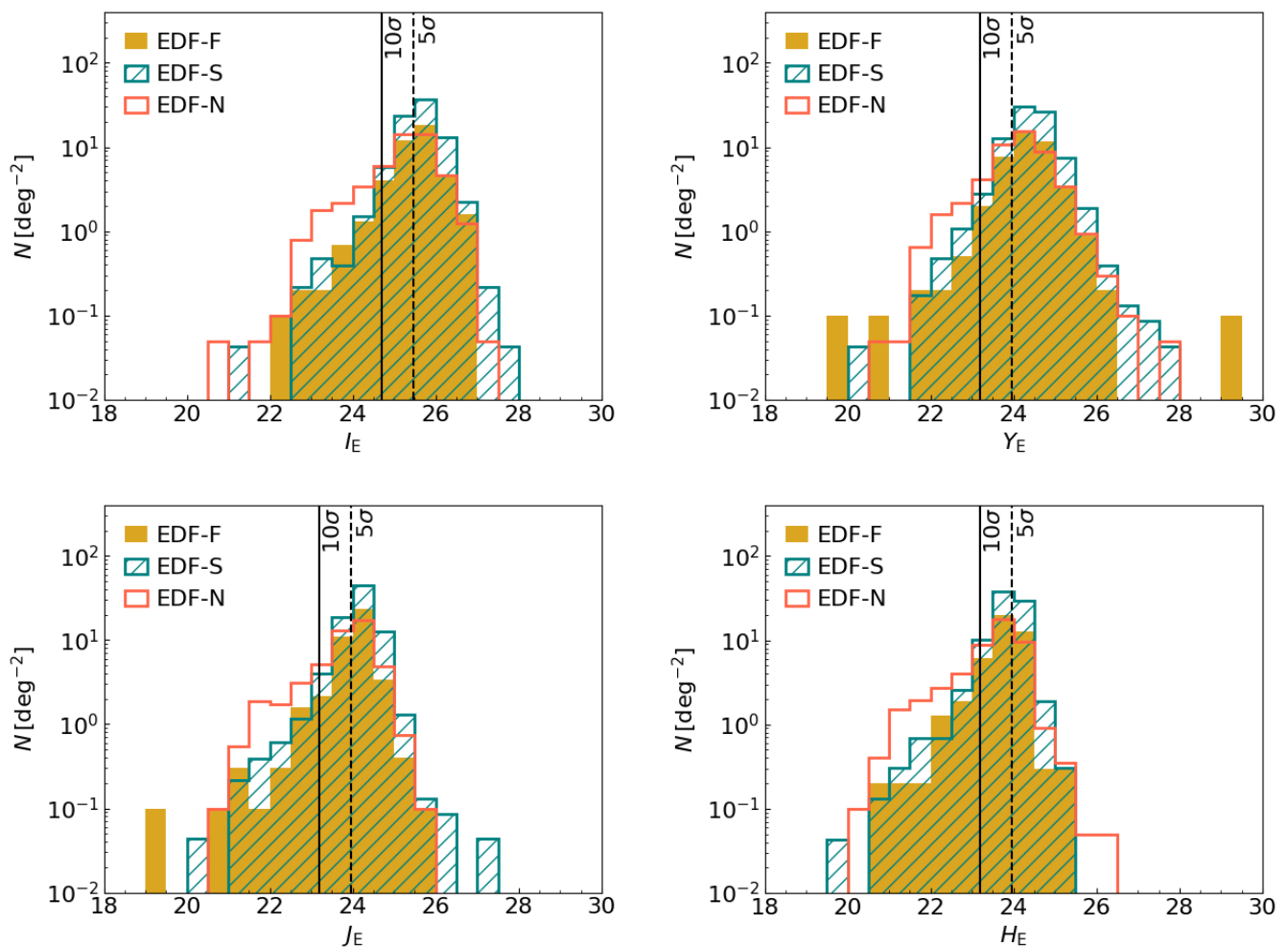


Fig. 4. Magnitude density distribution of the LRD candidates in the three fields in the four *Euclid* filters. The black vertical solid and dashed lines indicate the 10σ and 5σ depths, respectively.

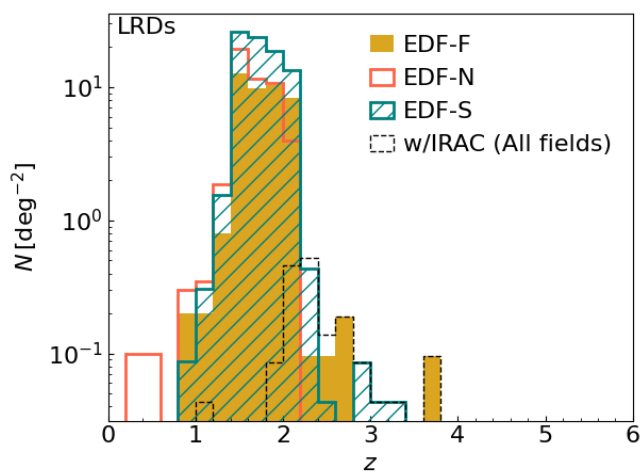


Fig. 5. Photometric redshift distribution of the samples of LRD candidates in the three EDFs. The black dotted histogram shows the overall distribution of sources detected in IRAC.

these objects are inside the selection criteria by Donley et al. (2012).

4.3.3. Spectroscopic selections

The EDF-N is partially covered by DESI EDR (DESI Collaboration et al. 2024), allowing for the classification of QSOs using spectroscopic data. This classification is also included in Euclid Collaboration: Matamoro Zatarain et al. (2025, Sect. 3.3.1) and two LRD candidates (0.2% of our sample in the EDF-N) are indeed classified as QSOs both by the DESI spectral type classification and looking at the DESI spectra, having $\text{FWHM} \geq 1200 \text{ km s}^{-1}$ in one of the hydrogen lines. Euclid Collaboration: Matamoro Zatarain et al. (2025) also includes other diagnostic based on spectroscopic DESI spectra, but no LRD candidates are selected by them.

4.3.4. X-ray AGN

We now compare our catalogue with the *Euclid* X-ray selected AGN catalogue (Euclid Collaboration: Roster et al. 2025). This catalogue lists the most likely *Euclid* counterparts to the 4XMM DR13, *Chandra* CSC 2.0, and eROSITA DR1 catalogue. While the former two cover the three *Euclid* field in a few, deep pointed observations, the latter covers EDF-F and EDF-S homogeneously but at a shallow depth (see figures 1 and 2 of Euclid Collaboration: Roster et al. 2025).

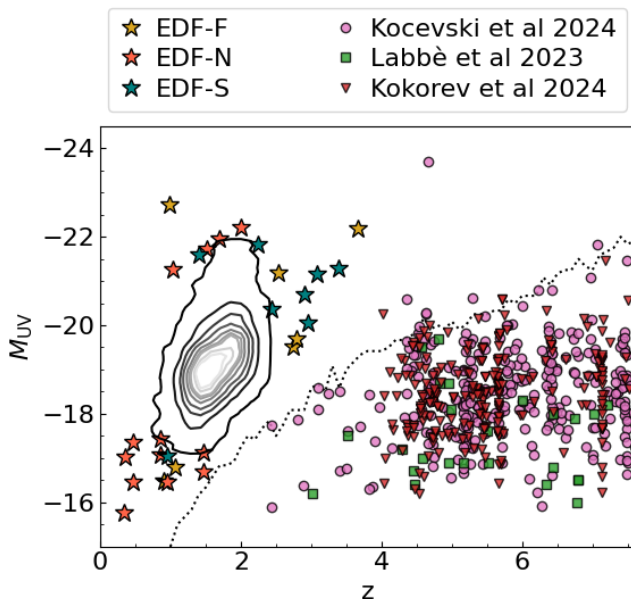


Fig. 6. M_{UV} and redshift for all LRD candidates, show as contour lines, equally spaced from 10% to 90% with the last one representing 99% of the distribution. The remaining 1% of the sample is shown with stars, colour-coded based on their field. We also show three samples of LRDs selected with JWST observations (Kocevski et al. 2024; Labbè et al. 2023; Kokorev et al. 2024a). The black dotted line show the 80% completeness expected once the EDFs are at their final depth.

Out of the entire sample of LRD candidates, three sources (0.09%) are present in the *Euclid* X-ray selected AGN catalogue, two in the EDF-S and one in the EDF-F. The two sources in the EDF-S are matched with sources in the eROSITA DR1, with a probability of being the right counterparts of $p_{\text{any}} = 0.16$ and 0.97. The source in the EDF-F is matched with a X-ray source in the *Chandra* CSC 2.0 catalogue with a probability of being the right counterparts of $p_{\text{any}} = 0.98$. For these sources the chance association can be higher than 80% (see Fig. 7 in Euclid Collaboration: Roster et al. 2025). Out of the three matches, only one has $S/N > 3$ at (0.5–2.3) keV, that is $f_{0.5-2.3\text{keV}} = (3.92 \pm 1.08) \times 10^{-14} \text{ erg s}^{-1} \text{ cm}^{-2}$, corresponding to a luminosity of $2.61 \times 10^{44} \text{ erg s}^{-1}$ at of $z_{\text{phot}} = 1.1$. A second source has instead a $S/N = 2$ at (0.5–2.3) keV, that is $f_{0.5-2.3\text{keV}} = (1.24 \pm 0.62) \times 10^{-14} \text{ erg s}^{-1} \text{ cm}^{-2}$, while the third one is below $S/N < 1$, with a 3σ upper limit of $f_{0.5-2.3\text{keV}} = 5.06 \times 10^{-16} \text{ erg s}^{-1} \text{ cm}^{-2}$.

Euclid Collaboration: Roster et al. (2025) also identify potential X-ray emitters, using a combination of Bayesian statistics and machine learning. This classification allows us to identify potential X-ray emitters outside the area covered by X-ray observations, which may be useful, for example, for follow up studies. There are no LRD candidates that are classified as potential X-ray emitters.

Overall, the small fraction of X-ray LRD candidates of this work is in line with previous works, showing that the majority of LRD are X-ray weak (e.g., Yue et al. 2024), but it is necessary to consider that the X-ray surveys considered here are shallower than the one used to matched previous LRDs selected with JWST. Further analysis of the X-ray emission of these sources in the future could shed light on the AGN contribution in LRDs.

A reassuring result is that all X-ray LRDs have a probability of less than 1% of being Galactic sources. This probability was derived by Euclid Collaboration: Roster et al. (2025) using a random forest algorithm trained on the methodology described in Salvato et al. (2022).

4.3.5. Comparison of the different selections

The number of LRD candidates selected as QSO in the EDF-F and EDF-S is shown in Fig. 7, showing also the overlap between the different selections. No sources are identified by all selections, while 1898 (80% of EDF-F and EDF-S) are selected by at least one criterion. The number of LRD candidates selected as QSO in the EDF-N is instead shown in Fig. 8, showing also the overlap between the different selections. Overall, 816, which corresponds to 84% of the EDF-N sample of LRDs, is selected by at least one criterion, while no sources are selected by all criteria.

Considering that LRDs may host an AGN and present a blue UV rest-frame continuum, it is not surprising that they are selected by QSO criteria. Follow-up studies are therefore fundamental to confirm the nature of these sources.

4.4. LRDs luminosity function

To measure the UV luminosity function of our sample of LRD candidates, we used the $1/V_{\text{max}}$ method (Rowan-Robinson 1968; Schmidt 1968). In particular, for each magnitude and redshift bin the luminosity function is defined as

$$\Phi(M)dM = \frac{1}{\Delta M} \sum_i^N \frac{1}{w_i V_{\text{max},i}}, \quad (3)$$

where ΔM is the width of the magnitude bin, w_i is the completeness correction for the i th object, and $V_{\text{max},i}$ is the maximum comoving volume at which object i could have been detected. To calculate the latter, we need to consider the area covered by the observations, the minimum redshift of the bin and the maximum redshift at which each source could be observed. The latter is derived considering the v-shaped model of each source, described by two power laws with slopes $\beta_{UV,i}$ and $\beta_{opt,i}$, normalised to the absolute UV magnitude ($M_{UV,i}$). This model is then shifted from the minimum to the maximum redshift of the redshift bin, and at each redshift step it is convolved with the *Euclid* and ancillary bands to estimate the expected fluxes. These fluxes are then used to derive the maximum redshift at which we would have at least four filters with $S/N > 3$.

4.4.1. Area

The area associated with each field has been derived considering the coverage map for the four *Euclid* filters, combined to remove the area in which at least one filter has been masked. In addition, we also removed additional masked areas covering bright stars, both halo and ground bleeding trails, as well as extended bright foreground sources. In addition, we combined these masks with the coverage by IRAC to derive the area associated with IRAC-detected sources. The areas considered are listed in Table 5.

4.4.2. Completeness limits and correction

To derive the 80% completeness limit of our sample, we derived the fraction of LRDs having at least four filters with $S/N > 3$

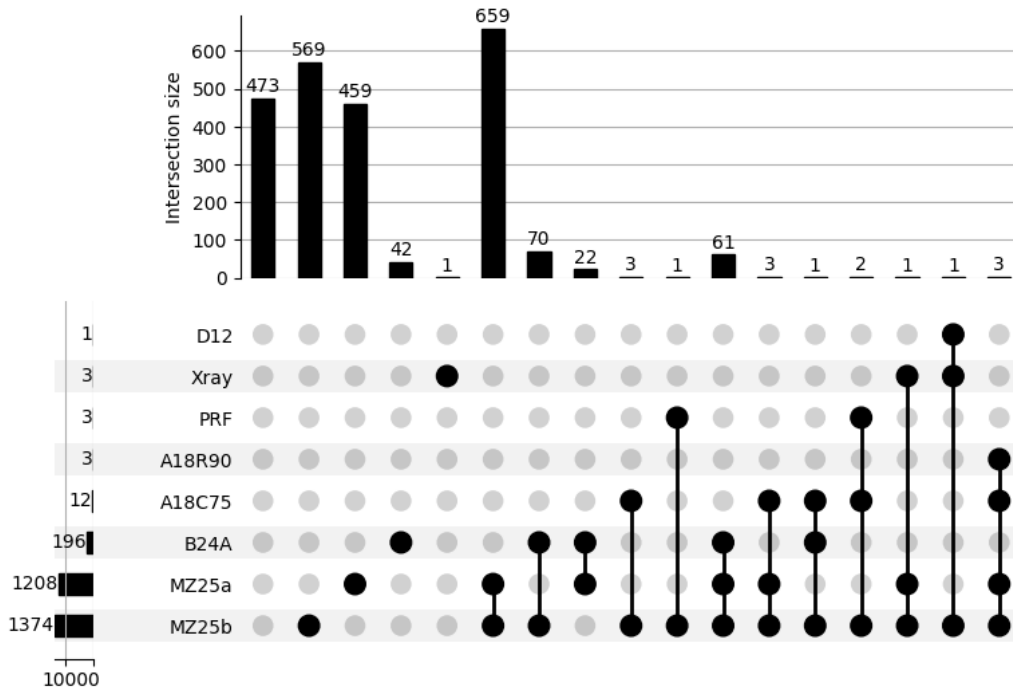


Fig. 7. UpSet plot showing the the intersections of all QSO selection methods reported by [Euclid Collaboration: Matamoro Zatarain et al. \(2025\)](#), out of 2370 LRD candidates in the EDF-F and EDF-S.

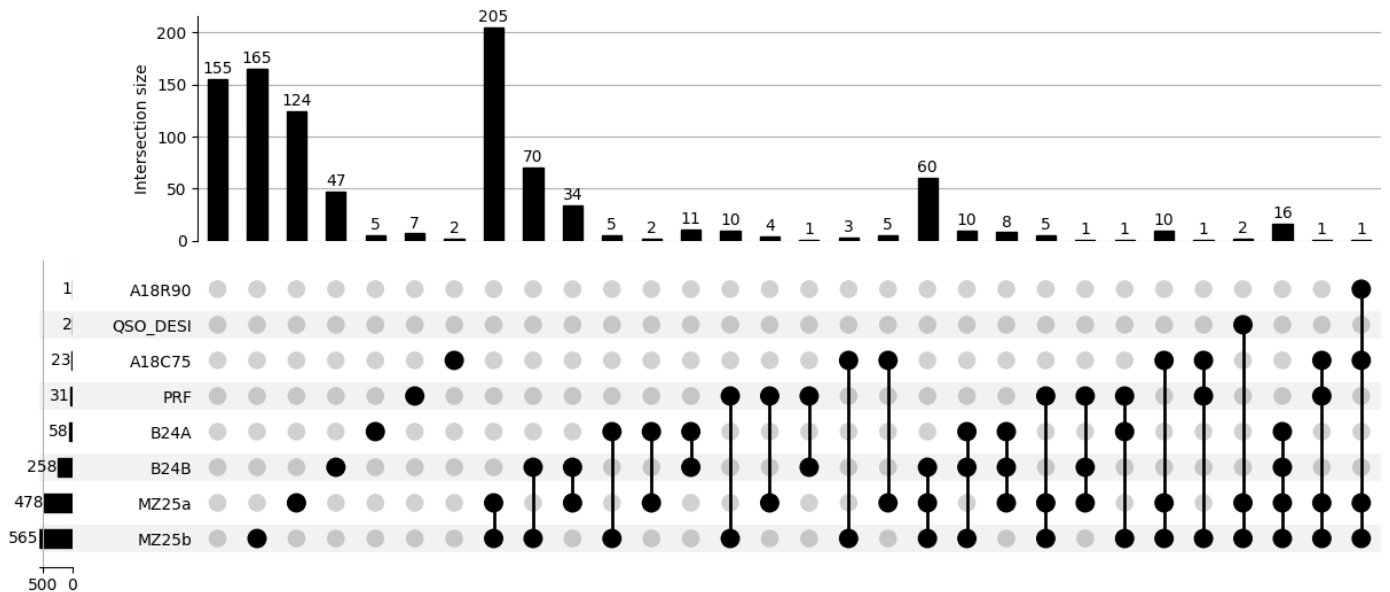


Fig. 8. UpSet plot showing the the intersections of all QSO selection methods reported by [Euclid Collaboration: Matamoro Zatarain et al. \(2025\)](#) and X-ray sources by [Euclid Collaboration: Roster et al. \(2025\)](#), out of 971 LRD candidates in the EDF-N.

Table 5. Area in deg^2 used to estimate the LRD luminosity function.

	EDF-F	EDF-N	EDF-S
After masking	11.85	19.76	26.16
w/IRAC	2.57	13.46	21.10

as a function of both redshift and M_{UV} . In particular, we considered redshift bins of $\Delta z = 0.25$ up to $z = 6$, since no LRDs are found at higher redshifts. We also considered magnitude bins of $\Delta M_{UV} = 0.25$ from $M_{UV} = -25$ to $M_{UV} = -10$. In each redshift-

magnitude bin, we randomly extracted 1000 β_{UV} and β_{opt} values from the observed distribution. We then derived the fraction of these mock LRDs that are observed in at least four filters with $S/N > 3$, considering the depths of the different fields reported in [Table 1](#). We used this estimate to correct the derived luminosity function.

In addition, we also applied the corrections for wrong redshifts, derived from the analysis of the redshift recovery on the simulated sample in [Appendix B](#). This is a correction that varies from 0.6 for $z = 1-1.5$, since the number of sources in this redshift range is expected to be overestimated, to 1.3 for $z = 2-2.5$, where instead the number of objects is underestimated. A more

detailed completeness correction, taking into account for example the compactness of the sources, will be estimated in future works, once the systematic effects of the telescope are better understood.

4.4.3. Uncertainties

We estimated the uncertainties of the luminosity function by performing a bootstrap analysis of the sample, generating 100 random samples starting from the entire LRD sample. In addition, on every realisation, we randomized both the redshift and the absolute UV magnitude considering a Gaussian function centred on the best-fit value and with standard deviation equal to their respective uncertainties. We added in quadrature to these uncertainties the Poisson errors following the prescription by [Gehrels \(1986\)](#). We do not include any uncertainty due to cosmic variance.

4.4.4. Estimated luminosity functions

We derived the UV luminosity functions of LRDs as explained in the previous sections and considering the following redshift bins: $0.6 \leq z < 1.0$; $1.0 \leq z < 1.5$; $1.5 \leq z < 2.0$; $2.0 \leq z < 2.5$; and $2.5 \leq z < 4.0$. In the first redshift bin we considered only objects in EDF-N, as the other fields lack the u band observations necessary to properly trace the UV slope. 11 objects (0.3% of the sample) are not considered in the UV luminosity functions because they correspond to a redshift where the UV slope is not properly covered. The derived UV luminosity functions are shown in [Fig. 9](#), where we also compare our results with UV luminosity functions from the literature of both LRDs, based on JWST data ([Kokorev et al. 2024a](#); [Kocevski et al. 2024](#)), and QSO, including JWST data ([Maiolino et al. 2024b](#); [Harikane et al. 2023](#); [Grazian et al. 2024](#)) or before JWST ([Giallongo et al. 2012](#); [McGreer et al. 2013](#); [Giallongo et al. 2015](#); [Akiyama et al. 2018](#); [Niida et al. 2020](#); [Pan et al. 2022](#)). The values of the LRD luminosity function of this work are also reported in [Table 6](#).

In the highest redshift bin (i.e., $4.0 \leq z < 6.0$) no candidates are found, making comparisons with previous JWST results impossible. We must therefore wait for future *Euclid* releases to improve over these results.

At redshifts $z < 4$ we can compare only to previous QSO UV luminosity functions, since observations of LRDs with JWST were mainly limited to $z > 4$. The luminosity function of the LRDs is always well below the QSO luminosity functions at bright magnitudes, indicating that LRDs are not the dominant AGN population at these magnitudes at $z < 4$, assuming they are AGN. The LRD luminosity functions are instead closer to the QSO ones at $z > 1$ and at the faintest magnitudes probed by this work.

In the same figure we also report the maximum volume probed by one of the largest JWST survey so far, that is COSMOS-Web ([Casey et al. 2023](#)) covering 0.6 deg^2 (red dotted line in [Fig. 9](#)), and the Cosmic Assembly Near-infrared Deep Extragalactic Legacy Survey (CANDELS [Grogin et al. 2011](#)) covering 0.29 deg^2 with *Hubble* Space Telescope (HST, red dash-dotted line in [Fig. 9](#)). At $z < 1$ and $z > 2.5$ the area of these two surveys are too small to observe a significant with luminosities similar to the candidates selected in this work. However, we would expect to observe some objects at the other redshifts: 17^{+8}_{-7} at $1.0 \leq z < 1.5$; 62^{+16}_{-17} at $1.5 \leq z < 2.0$; and 15^{+4}_{-5} at $2.0 \leq z < 2.5$ in CANDELS; 31^{+15}_{-13} at $1.0 \leq z < 1.5$; 116^{+30}_{-31} at $1.5 \leq z < 2.0$; and 29^{+7}_{-9} at $2.0 \leq z < 2.5$ in COSMOS-Web. However, at these

redshifts, no LRD was identified with HST and few with JWST. For example, [Kocevski et al. \(2024\)](#) found 17 LRD candidates at $z < 4$, while in the same area, given the LRD luminosity function found in this work, we would expect 53^{+10}_{-11} candidates. This difference (2σ deviation) in number density may be due to contaminants or may be due to the different angular resolution of *Euclid* and JWST, making future follow-up studies fundamental. However, it is important to notice that the subsample of more robust LRD candidates, that are the one observed also by IRAC, have a number density too low to be detected by any JWST or HST survey.

We also report the conservative luminosity function derived only with the IRAC-detected sources, which have more constraints but have also been more heavily cleaned to avoid blending issues. This estimations are compatible with the few LRD candidates at $z < 4$ observed by JWST and HST.

A comparison between the LRDs UV luminosity functions derived in this work is shown in [Fig. 10](#). From this plot it is possible to identify a tentative evolution of the luminosity function with redshift. Indeed, the density of LRD candidates increases from the high redshift down to $z = 1.5$ – 2.5 and decreases at even lower redshifts, resembling the evolution of the full population of star-forming galaxies and QSOs. While the statistics in the lowest redshift bin are quite poor, since it is based on the EDF-N only, the number of sources at $1.0 \leq z < 1.5$ is statistically significant. However, the density of LRD candidates with $M_{\text{UV}} \geq -21$ at $1 \leq z < 2.5$ is similar to the one derived with JWST at $4 \leq z < 6$ ([Kocevski et al. 2024](#); [Kokorev et al. 2024a](#)), indicating that part of the high- z evolution could be due to incompleteness in our LRD sample. This evolution is not present if we consider only the few LRD candidates detected in IRAC, as statistic is too low.

Further analysis is needed to understand the level of contamination in our sample or why these LRD candidates have been missed by previous JWST studies. A possibility could also be that these sources are not as compact as the ones observed with JWST, being compact when considering *Euclid* spatial resolution, but not with JWST, which is 4–6 times better than the *Euclid*'s. In the future, as the depth of the EDFs increases and the spectroscopic coverage improves, the identification of LRDs and the estimation of their properties will improve, making it possible to derive more conclusive results on the possible redshift evolution of the LRD luminosity function.

5. Conclusions

In this work we have taken advantage of the *Euclid* Q1 data covering around 63 deg^2 to search for LRD candidates. The selection was performed exploiting *Euclid* photometric data, ground-based ancillary data, and Spitzer/IRAC data. After a conservative selection, including conservative flagging and careful visual inspection of all candidates, we obtained a final sample of 3341 LRD candidates, 29 of which are detected also with IRAC.

Even if we impose a $S/N > 3$ in at least four filters, LRD candidates are relatively faint, with mean magnitudes of $I_E = 25.5$, $Y_E = 24.3$, $J_E = 24.0$, and $H_E = 23.7$, which are fainter than the 5σ limits of the Q1 data release. Their photometric redshift has been estimated to range between $z = 0.33$ and $z = 3.6$, where previous JWST selections identified a strong decrease of LRD candidates. However, at $z > 4$, the depth of the ancillary IRAC data limit our sample to only the brightest sources.

We also derived the rest-frame UV luminosity function, but no overlap is present in the parameter space of *Euclid* and JWST, limiting direct comparison. Indeed, *Euclid* is complementary to

Table 6. UV luminosity function of LRD candidates.

M_{UV}	$0.6 \leq z < 1.0$	$1.0 \leq z < 1.5$	$1.5 \leq z < 2.0$	$2.0 \leq z < 2.5$	$2.5 \leq z < 4.0$
-22.75	$-7.12^{+1.01}_{-0.57}$				
-22.25				$-7.89^{+1.03}_{-0.57}$	$-7.39^{+1.1}_{-0.57}$
-21.75		$-7.76^{+2.12}_{-0.4}$	$-7.0^{+0.47}_{-0.17}$	$-7.46^{+0.99}_{-0.24}$	
-21.25		$-7.46^{+1.53}_{-0.38}$	$-6.55^{+0.38}_{-0.11}$	$-6.88^{+0.24}_{-0.25}$	$-7.29^{+0.66}_{-0.44}$
-20.75			$-6.39^{+0.42}_{-0.15}$	$-6.74^{+0.43}_{-0.13}$	$-8.28^{+1.17}_{-0.57}$
-20.25		$-7.33^{+3.71}_{-1.45}$	$-5.77^{+0.35}_{-0.22}$	$-6.09^{+0.3}_{-0.1}$	
-19.75		$-6.49^{+1.37}_{-0.79}$	$-5.27^{+0.22}_{-0.15}$	$-5.71^{+0.12}_{-0.04}$	
-19.25		$-5.61^{+0.06}_{-0.06}$	$-4.95^{+0.03}_{-0.06}$	$-5.66^{+0.09}_{-0.07}$	
-18.75		$-5.26^{+0.19}_{-0.24}$	$-4.96^{+0.11}_{-0.15}$	$-5.86^{+0.34}_{-0.11}$	
-18.25		$-5.49^{+0.12}_{-0.19}$	$-5.27^{+0.08}_{-0.14}$	$-7.26^{+2.72}_{-1.2}$	
-17.75		$-5.82^{+0.06}_{-0.16}$	$-6.06^{+0.52}_{-0.3}$		
-17.25		$-6.54^{+0.75}_{-0.23}$	$-6.92^{+2.46}_{-1.36}$		
-16.75		$-7.09^{+1.89}_{-0.64}$			
-16.25	$-7.12^{+1.03}_{-0.57}$				

Notes. The first column show the central value of the UV absolute magnitude bins, which are 0.5 mag wide. The other columns show the logarithm of the number density in $\text{Mpc}^{-3} \text{mag}^{-1}$ in different redshift bins, reported in the first row.

JWST observations because it can probe the bright-end of the UV luminosity function, thanks to the large area covered. The most puzzling result is that the UV luminosity function of LRD candidates increases from high z down to $z = 1.5$ – 2.5 , below which it decreases again. This is in contrast with previous JWST results which derived a drastic drop of LRDs at $z < 4$, with almost no candidates at $z < 2$. However, the $z > 4$ evolution of our luminosity function may be affected by incompleteness in our LRD candidates sample. It is important to note that no significant evolution is apparent focusing on the subsample of more robust LRD candidates having also IRAC detections, which however has poor statistics (only 29 objects) and is limited by the IRAC resolution. Clearly, more observations will be required to clarify this situation. Another interesting result is that the LRD UV luminosity function remains below the QSO one, except at $M_{UV} > -21$, where they become compatible. This could indicate that, if LRDs are indeed AGN, they are anyway a sub-dominant AGN population.

Further analyses are necessary to validate the LRD candidates of this work and optimise the removal of possible contaminants. In addition, further critical studies need to probe their structure and check for their compatibility with JWST sources, given the different spatial resolution of the two telescopes. If a sizeable fraction of the LRD candidates identified in this work are confirmed by future studies, it will enable us to study the redshift evolution over a broad redshift and luminosity range thus helping shedding light on these mysterious sources. Future *Euclid* data releases are expected to increase the number of LRD candidates, but also to increase the overlap in parameter space with previous JWST samples, as the *Euclid* Wide survey will be wider than the Q1 at similar depth, while the *Euclid* Deep survey will be considerably deeper. In addition, a direct comparison between JWST and *Euclid* selections will be possible in future releases, as *Euclid* will cover some of the area already observed with JWST.

Acknowledgements. The research activities described in this paper were carried out with contribution of the Next Generation EU funds within the National Recovery and Resilience Plan (PNRR), Mission 4 – Education and Research, Component 2 – From Research to Business (M4C2), Investment Line 3.1 – Strengthening

and creation of Research Infrastructures, Project IR0000034–“STILES – Strengthening the Italian Leadership in ELT and SKA”. This work has benefited from the support of Royal Society Research Grant RGS\R1\231450. This research was supported by the International Space Science Institute (ISSI) in Bern, through ISSI International Team project #23-573 “Active Galactic Nuclei in Next Generation Surveys”. L.B., F.R., and V.A acknowledge the support from the INAF Large Grant “AGN & Euclid: a close entanglement” Ob. Fu. 01.05.23.01.14. A.F. acknowledges the support from project “VLT- MOONS” CRAM 1.05.03.07, INAF Large Grant 2022 “The metal circle: a new sharp view of the baryon cycle up to Cosmic Dawn with the latest generation IFU facilities” and INAF Large Grant 2022 “Dual and binary SMBH in the multi-messenger era”. L.B. thanks A. Marasco for computational support. This research made use of Photutils, an Astropy package for detection and photometry of astronomical sources (Bradley et al. 2023). The Euclid Consortium acknowledges the European Space Agency and a number of agencies and institutes that have supported the development of *Euclid*, in particular the Agenzia Spaziale Italiana, the Austrian Forschungsgesellschaft funded through BMK, the Belgian Science Policy, the Canadian Euclid Consortium, the Deutsches Zentrum für Luft- und Raumfahrt, the DTU Space and the Niels Bohr Institute in Denmark, the French Centre National d’Etudes Spatiales, the Fundação para a Ciência e a Tecnologia, the Hungarian Academy of Sciences, the Ministerio de Ciencia, Innovación y Universidades, the National Aeronautics and Space Administration, the National Astronomical Observatory of Japan, the Nederlandse Onderzoeksschool Voor Astronomie, the Norwegian Space Agency, the Research Council of Finland, the Romanian Space Agency, the State Secretariat for Education, Research, and Innovation (SERI) at the Swiss Space Office (SSO), and the United Kingdom Space Agency. A complete and detailed list is available on the *Euclid* web site (www.euclid-ec.org). This work has made use of the *Euclid* Quick Release Q1 data from the *Euclid* mission of the European Space Agency (ESA), 2025, <https://doi.org/10.57780/esa-2853f3b>. This research makes use of ESA Datalabs (datalabs.esa.int), an initiative by ESA’s Data Science and Archives Division in the Science and Operations Department, Directorate of Science. Based on data from UNIONS, a scientific collaboration using three Hawaii-based telescopes: CFHT, Pan-STARRS, Subaru www.skysurvey.cc. Based on data from the Dark Energy Camera (DECam) on the Blanco 4-m Telescope at CTIO in Chile <https://www.darkenergysurvey.org>. This work uses results from the ESA mission *Gaia*, whose data are being processed by the Gaia Data Processing and Analysis Consortium <https://www.cosmos.esa.int/gaia>. This publication is based on observations made with the Spitzer Space Telescope, which is operated by the Jet Propulsion Laboratory, California Institute of Technology under a contract with NASA, and has made use of the NASA/IPAC Infrared Science Archive, which is funded by the National Aeronautics and Space Administration and operated by the California Institute of Technology.

References

- Abbott, T. M. C., Abdalla, F. B., Allam, S., et al. 2018, *ApJS*, 239, 18
- Akins, H. B., Casey, C. M., Lambrides, E., et al. 2024, arXiv e-prints, arXiv:2406.10341
- Akiyama, M., He, W., Ikeda, H., et al. 2018, *PASJ*, 70, S34
- Alexander, T. & Natarajan, P. 2014, *Science*, 345, 1330
- Ananna, T. T., Bogdán, Á., Kovács, O. E., Natarajan, P., & Hickox, R. C. 2024, *ApJ*, 969, L18
- Assef, R. J., Stern, D., Noirot, G., et al. 2018, *ApJS*, 234, 23
- Asthana, S., Haehnelt, M. G., Kulkarni, G., et al. 2024, arXiv e-prints, arXiv:2409.15453
- Atek, H., Labbé, I., Furtak, L. J., et al. 2024, *Nature*, 626, 975
- Baggen, J. F. W., van Dokkum, P., Brammer, G., et al. 2024, *ApJ*, 977, L13
- Barkana, R. & Loeb, A. 2001, *Phys. Rep.*, 349, 125
- Barro, G., Perez-Gonzalez, P. G., Kocevski, D. D., et al. 2024, arXiv e-prints, arXiv:2412.01887
- Barro, G., Perez-Gonzalez, P. G., Kocevski, D. D., et al. 2023, arXiv e-prints, arXiv:2305.14418
- Begelman, M. C. & Volonteri, M. 2017, *MNRAS*, 464, 1102
- Bellovary, J. 2025, arXiv e-prints, arXiv:2501.03309
- Bradley, L., Sipőcz, B., Robitaille, T., et al. 2023, *astropy/photutils*: 1.10.0
- Carr, B. J. & Hawking, S. W. 1974, *MNRAS*, 168, 399
- Casey, C. M., Kartaltepe, J. S., Drakos, N. E., et al. 2023, *ApJ*, 954, 31
- Dayal, P. 2024, *A&A*, 690, A182
- Dayal, P. & Ferrara, A. 2018, *Phys. Rep.*, 780, 1
- Dayal, P., Volonteri, M., Greene, J. E., et al. 2024, arXiv e-prints, arXiv:2401.11242
- Delvecchio, I., Daddi, E., Sargent, M. T., et al. 2022, *A&A*, 668, A81
- DESI Collaboration, Adame, A. G., Aguilar, J., et al. 2024, *AJ*, 168, 58
- Donley, J. L., Koekemoer, A. M., Brusa, M., et al. 2012, *ApJ*, 748, 142
- Euclid Collaboration: Aussel, H., Tereno, I., Schirmer, M., et al. 2025, *A&A*, submitted
- Euclid Collaboration: Bisigello, L., Massimo, M., Tortora, C., et al. 2024, *A&A*, 691, A1
- Euclid Collaboration: Cropper, M., Al Bahlawan, A., Amiaux, J., et al. 2024, *A&A*, accepted, arXiv:2405.13492
- Euclid Collaboration: Jahnke, K., Gillard, W., Schirmer, M., et al. 2024, *A&A*, accepted, arXiv:2405.13493
- Euclid Collaboration: Margalef-Bentabol, B., Wang, L., La Marca, A., et al. 2025, *A&A*, submitted
- Euclid Collaboration: Matamoros Zatarain, T., Fotopoulou, S., Ricci, F., et al. 2025, *A&A*, submitted
- Euclid Collaboration: McCracken, H., Benson, K., et al. 2025, *A&A*, submitted
- Euclid Collaboration: McPartland, C. J. R., Zalesky, L., Weaver, J. R., et al. 2024, *A&A*, submitted, arXiv:2408.05275
- Euclid Collaboration: Mellier, Y., Abdurro'uf, Acevedo Barroso, J., et al. 2024, *A&A*, accepted, arXiv:2405.13491
- Euclid Collaboration: Moneti, A., McCracken, H. J., Shuntov, M., et al. 2022, *A&A*, 658, A126
- Euclid Collaboration: Polenta, G., Frailis, M., Alavi, A., et al. 2025, *A&A*, submitted
- Euclid Collaboration: Romelli, E., Kümmel, M., Dole, H., et al. 2025, *A&A*, submitted
- Euclid Collaboration: Roster, W., Salvato, M., Buchner, J., et al. 2025, *A&A*, submitted
- Euclid Collaboration: Tucci, M., Paltani, S., Hartley, W., et al. 2025, *A&A*, submitted
- Euclid Collaboration: Zalesky, L., McPartland, C. J. R., Weaver, J. R., et al. 2024, *A&A*, submitted, arXiv:2408.05296
- Euclid Quick Release Q1. 2025, <https://doi.org/10.57780/esa-2853f3b>
- Ferrarese, L. 2002, *ApJ*, 578, 90
- Fumagalli, M., Patel, S. G., Franx, M., et al. 2012, *ApJ*, 757, L22
- Furtak, L. J., Zitrin, A., Plat, A., et al. 2023, *ApJ*, 952, 142
- Gaia Collaboration: Vallenari, A., Brown, A. G. A., Prusti, T., et al. 2023, *A&A*, 674, A1
- Gebhardt, K., Bender, R., Bower, G., et al. 2000, *ApJ*, 539, L13
- Gehrels, N. 1986, *ApJ*, 303, 336
- Giallongo, E., Grazian, A., Fiore, F., et al. 2015, *A&A*, 578, A83
- Giallongo, E., Menci, N., Fiore, F., et al. 2012, *ApJ*, 755, 124
- Glikman, E., Simmons, B., Maily, M., et al. 2015, *ApJ*, 806, 218
- Glikman, E., Urrutia, T., Lacy, M., et al. 2012, *ApJ*, 757, 51
- Gordon, K. D., Clayton, G. C., Declair, M., et al. 2023, *ApJ*, 950, 86
- Grazian, A., Giallongo, E., Boutsia, K., et al. 2024, *ApJ*, 974, 84
- Greene, J. E., Labbe, I., Goulding, A. D., et al. 2024, *ApJ*, 964, 39
- Grogin, N. A., Kocevski, D. D., Faber, S. M., et al. 2011, *The Astrophysical Journal Supplement Series*, 197, 35
- Gültekin, K., Richstone, D. O., Gebhardt, K., et al. 2009, *ApJ*, 698, 198
- Habouzit, M., Li, Y., Somerville, R. S., et al. 2021, *MNRAS*, 503, 1940
- Habouzit, M., Pisani, A., Goulding, A., et al. 2020, *MNRAS*, 493, 899
- Hainline, K. N., Maiolino, R., Juodžbalis, I., et al. 2024, arXiv e-prints, arXiv:2410.00100
- Harikane, Y., Zhang, Y., Nakajima, K., et al. 2023, *ApJ*, 959, 39
- Hawking, S. 1971, *MNRAS*, 152, 75
- Hickox, R. C. & Alexander, D. M. 2018, *ARA&A*, 56, 625
- Inayoshi, K., Haiman, Z., & Ostriker, J. P. 2016, *MNRAS*, 459, 3738
- Inayoshi, K. & Maiolino, R. 2024, arXiv e-prints, arXiv:2409.07805
- Juodžbalis, I., Ji, X., Maiolino, R., et al. 2024, *MNRAS*, 535, 853
- Killi, M., Watson, D., Brammer, G., et al. 2024, *A&A*, 691, A52
- Kocevski, D. D., Finkelstein, S. L., Barro, G., et al. 2024, arXiv e-prints, arXiv:2404.03576
- Kocevski, D. D., Onoue, M., Inayoshi, K., et al. 2023, *ApJ*, 954, L4
- Kokorev, V., Caputi, K. I., Greene, J. E., et al. 2024a, *ApJ*, 968, 38
- Kokorev, V., Chisholm, J., Endsley, R., et al. 2024b, *ApJ*, 975, 178
- Kokubo, M. & Harikane, Y. 2024, arXiv e-prints, arXiv:2407.04777
- Kulkarni, G., Worseck, G., & Hennawi, J. F. 2019, *MNRAS*, 488, 1035
- Labbe, I., Greene, J. E., Bezanson, R., et al. 2023, arXiv e-prints, arXiv:2306.07320
- Labbe, I., van Dokkum, P., Nelson, E., et al. 2023, *Nature*, 616, 266
- Langeroodi, D. & Hjorth, J. 2023, *ApJ*, 957, L27
- Lin, R., Zheng, Z.-Y., Jiang, C., et al. 2024, arXiv e-prints, arXiv:2412.08396
- Madau, P., Giallongo, E., Grazian, A., & Haardt, F. 2024, *ApJ*, 971, 75
- Magorrian, J., Tremaine, S., Richstone, D., et al. 1998, *ApJ*, 115, 2285
- Maiolino, R., Risaliti, G., Signorini, M., et al. 2024a, arXiv e-prints, arXiv:2405.00504
- Maiolino, R., Scholtz, J., Curtis-Lake, E., et al. 2024b, *A&A*, 691, A145
- Maiolino, R., Scholtz, J., Witstok, J., et al. 2024c, *Nature*, 627, 59
- Matthee, J., Naidu, R. P., Brammer, G., et al. 2024, *ApJ*, 963, 129
- Mazzolari, G., Gilli, R., Maiolino, R., et al. 2024, arXiv e-prints, arXiv:2412.04224
- McGreer, I. D., Jiang, L., Fan, X., et al. 2013, *ApJ*, 768, 105
- Mezcua, M., Pacucci, F., Suh, H., Siudek, M., & Natarajan, P. 2024, *ApJ*, 966, L30
- Mullaney, J. R., Daddi, E., Béthermin, M., et al. 2012, *ApJ*, 753, L30
- Netzer, H. 2015, *ARA&A*, 53, 365
- Niida, M., Nagao, T., Ikeda, H., et al. 2020, *ApJ*, 904, 89
- Noboriguchi, A., Inoue, A. K., Nagao, T., Toba, Y., & Misawa, T. 2023, *ApJ*, 959, L14
- Oke, J. B. & Gunn, J. E. 1983, *ApJ*, 266, 713
- Pacucci, F. & Loeb, A. 2022, *MNRAS*, 509, 1885
- Pacucci, F., Natarajan, P., Volonteri, M., Cappelluti, N., & Urry, C. M. 2017, *ApJ*, 850, L42
- Pan, Z., Jiang, L., Fan, X., Wu, J., & Yang, J. 2022, *ApJ*, 928, 172
- Pérez-González, P. G., Barro, G., Rieke, G. H., et al. 2024, *ApJ*, 968, 4
- Reis, I., Baron, D., & Shahaf, S. 2019, *AJ*, 157, 16
- Richards, G. T., Hall, P. B., Vanden Berk, D. E., et al. 2003, *AJ*, 126, 1131
- Rigby, J., Perrin, M., McElwain, M., et al. 2023, *Publications of the Astronomical Society of the Pacific*, 135, 048001
- Rowan-Robinson, M. 1968, *MNRAS*, 138, 445
- Salvato, M., Wolf, J., Dwelly, T., et al. 2022, *A&A*, 661, A3
- Schmidt, M. 1968, *ApJ*, 151, 393
- Silk, J. & Rees, M. J. 1998, *A&A*, 331, L1
- Simmonds, C., Tacchella, S., Hainline, K., et al. 2024, *MNRAS*, 535, 2998
- Stepney, M., Banerji, M., Tang, S., et al. 2024, *MNRAS*, 533, 2948
- Tanaka, T. S., Silverman, J. D., Shimasaku, K., et al. 2024, arXiv e-prints, arXiv:2412.14246
- Tee, W. L., Fan, X., Wang, F., & Yang, J. 2024, arXiv e-prints, arXiv:2412.05242
- Urrutia, T., Lacy, M., & Becker, R. H. 2008, *ApJ*, 674, 80
- Virtanen, P., Gommers, R., Oliphant, T. E., et al. 2020, *Nature Methods*, 17, 261
- Wang, B., Leja, J., de Graaff, A., et al. 2024, *ApJ*, 969, L13
- Webster, R. L., Francis, P. J., Petersont, B. A., Drinkwater, M. J., & Masci, F. J. 1995, *Nature*, 375, 469
- Wethers, C. F., Banerji, M., Hewett, P. C., et al. 2018, *MNRAS*, 475, 3682
- Williams, C. C., Alberts, S., Ji, Z., et al. 2024, *ApJ*, 968, 34
- Wyithe, J. S. B. & Loeb, A. 2012, *MNRAS*, 425, 2892
- Yue, M., Eilers, A.-C., Ananna, T. T., et al. 2024, *ApJ*, 974, L26
- Zhang, Z., Jiang, L., Liu, W., & Ho, L. C. 2024, arXiv e-prints, arXiv:2411.02729

¹ INAF-Osservatorio Astronomico di Padova, Via dell'Osservatorio 5, 35122 Padova, Italy

² Dipartimento di Fisica e Astronomia "G. Galilei", Università di Padova, Via Marzolo 8, 35131 Padova, Italy

³ School of Physics, HH Wills Physics Laboratory, University of Bristol, Tyndall Avenue, Bristol, BS8 1TL, UK

⁴ Department of Mathematics and Physics, Roma Tre University, Via della Vasca Navale 84, 00146 Rome, Italy

- ⁵ INAF-Osservatorio Astronomico di Roma, Via Frascati 33, 00078 Monteporzio Catone, Italy
- ⁶ Max-Planck-Institut für Astronomie, Königstuhl 17, 69117 Heidelberg, Germany
- ⁷ INAF-Osservatorio Astrofisico di Arcetri, Largo E. Fermi 5, 50125, Firenze, Italy
- ⁸ INAF-Osservatorio Astronomico di Capodimonte, Via Moiariello 16, 80131 Napoli, Italy
- ⁹ School of Physics & Astronomy, University of Southampton, Highfield Campus, Southampton SO17 1BJ, UK
- ¹⁰ Jeremiah Horrocks Institute, University of Central Lancashire, Preston, PR1 2HE, UK
- ¹¹ Dipartimento di Fisica e Astronomia "G. Galilei", Università di Padova, Vicolo dell'Osservatorio 3, 35122 Padova, Italy
- ¹² INAF, Istituto di Radioastronomia, Via Piero Gobetti 101, 40129 Bologna, Italy
- ¹³ Institute of Cosmology and Gravitation, University of Portsmouth, Portsmouth PO1 3FX, UK
- ¹⁴ Cavendish Laboratory, University of Cambridge, JJ Thomson Avenue, Cambridge, CB3 0HE, UK
- ¹⁵ Institute of Space Sciences (ICE, CSIC), Campus UAB, Carrer de Can Magrans, s/n, 08193 Barcelona, Spain
- ¹⁶ Institut d'Estudis Espacials de Catalunya (IEEC), Edifici RDIT, Campus UPC, 08860 Castelldefels, Barcelona, Spain
- ¹⁷ Max Planck Institute for Extraterrestrial Physics, Giessenbachstr. 1, 85748 Garching, Germany
- ¹⁸ Instituto de Astrofísica de Canarias (IAC); Departamento de Astrofísica, Universidad de La Laguna (ULL), 38200, La Laguna, Tenerife, Spain
- ¹⁹ Department of Astronomy, University of Geneva, ch. d'Ecogia 16, 1290 Versoix, Switzerland
- ²⁰ Department of Physical Sciences, Ritsumeikan University, Kusatsu, Shiga 525-8577, Japan
- ²¹ National Astronomical Observatory of Japan, 2-21-1 Osawa, Mitaka, Tokyo 181-8588, Japan
- ²² Academia Sinica Institute of Astronomy and Astrophysics (ASIAA), 11F of ASMA, No. 1, Section 4, Roosevelt Road, Taipei 10617, Taiwan
- ²³ SRON Netherlands Institute for Space Research, Landleven 12, 9747 AD, Groningen, The Netherlands
- ²⁴ Kapteyn Astronomical Institute, University of Groningen, PO Box 800, 9700 AV Groningen, The Netherlands
- ²⁵ INAF-Osservatorio di Astrofisica e Scienza dello Spazio di Bologna, Via Piero Gobetti 93/3, 40129 Bologna, Italy
- ²⁶ Sterrenkundig Observatorium, Universiteit Gent, Krijgslaan 281 S9, 9000 Gent, Belgium
- ²⁷ STAR Institute, University of Liège, Quartier Agora, Allée du six Août 19c, 4000 Liège, Belgium
- ²⁸ INAF-Istituto di Astrofisica e Planetologia Spaziali, via del Fosso del Cavaliere, 100, 00100 Roma, Italy
- ²⁹ Dipartimento di Fisica e Astronomia "Augusto Righi" - Alma Mater Studiorum Università di Bologna, via Piero Gobetti 93/2, 40129 Bologna, Italy
- ³⁰ Université Paris-Saclay, CNRS, Institut d'astrophysique spatiale, 91405, Orsay, France
- ³¹ ESAC/ESA, Camino Bajo del Castillo, s/n., Urb. Villafranca del Castillo, 28692 Villanueva de la Cañada, Madrid, Spain
- ³² School of Mathematics and Physics, University of Surrey, Guildford, Surrey, GU2 7XH, UK
- ³³ INAF-Osservatorio Astronomico di Brera, Via Brera 28, 20122 Milano, Italy
- ³⁴ Université Paris-Saclay, Université Paris Cité, CEA, CNRS, AIM, 91191, Gif-sur-Yvette, France
- ³⁵ IFPU, Institute for Fundamental Physics of the Universe, via Beirut 2, 34151 Trieste, Italy
- ³⁶ INAF-Osservatorio Astronomico di Trieste, Via G. B. Tiepolo 11, 34143 Trieste, Italy
- ³⁷ INFN, Sezione di Trieste, Via Valerio 2, 34127 Trieste TS, Italy
- ³⁸ SISSA, International School for Advanced Studies, Via Bonomea 265, 34136 Trieste TS, Italy
- ³⁹ Dipartimento di Fisica e Astronomia, Università di Bologna, Via Gobetti 93/2, 40129 Bologna, Italy
- ⁴⁰ INFN-Sezione di Bologna, Viale Berti Pichat 6/2, 40127 Bologna, Italy
- ⁴¹ Centre National d'Etudes Spatiales – Centre spatial de Toulouse, 18 avenue Edouard Belin, 31401 Toulouse Cedex 9, France
- ⁴² Universitäts-Sternwarte München, Fakultät für Physik, Ludwig-Maximilians-Universität München, Scheinerstrasse 1, 81679 München, Germany
- ⁴³ Space Science Data Center, Italian Space Agency, via del Politecnico snc, 00133 Roma, Italy
- ⁴⁴ Dipartimento di Fisica, Università di Genova, Via Dodecaneso 33, 16146, Genova, Italy
- ⁴⁵ INFN-Sezione di Genova, Via Dodecaneso 33, 16146, Genova, Italy
- ⁴⁶ Department of Physics "E. Pancini", University Federico II, Via Cinthia 6, 80126, Napoli, Italy
- ⁴⁷ Instituto de Astrofísica e Ciências do Espaço, Universidade do Porto, CAUP, Rua das Estrelas, PT4150-762 Porto, Portugal
- ⁴⁸ Faculdade de Ciências da Universidade do Porto, Rua do Campo de Alegre, 4150-007 Porto, Portugal
- ⁴⁹ Dipartimento di Fisica, Università degli Studi di Torino, Via P. Giuria 1, 10125 Torino, Italy
- ⁵⁰ INFN-Sezione di Torino, Via P. Giuria 1, 10125 Torino, Italy
- ⁵¹ INAF-Osservatorio Astrofisico di Torino, Via Osservatorio 20, 10025 Pino Torinese (TO), Italy
- ⁵² European Space Agency/ESTEC, Keplerlaan 1, 2201 AZ Noordwijk, The Netherlands
- ⁵³ Institute Lorentz, Leiden University, Niels Bohrweg 2, 2333 CA Leiden, The Netherlands
- ⁵⁴ Leiden Observatory, Leiden University, Einsteinweg 55, 2333 CC Leiden, The Netherlands
- ⁵⁵ INAF-IASF Milano, Via Alfonso Corti 12, 20133 Milano, Italy
- ⁵⁶ Centro de Investigaciones Energéticas, Medioambientales y Tecnológicas (CIEMAT), Avenida Complutense 40, 28040 Madrid, Spain
- ⁵⁷ Port d'Informació Científica, Campus UAB, C. Albareda s/n, 08193 Bellaterra (Barcelona), Spain
- ⁵⁸ Institute for Theoretical Particle Physics and Cosmology (TTK), RWTH Aachen University, 52056 Aachen, Germany
- ⁵⁹ INFN section of Naples, Via Cinthia 6, 80126, Napoli, Italy
- ⁶⁰ Institute for Astronomy, University of Hawaii, 2680 Woodlawn Drive, Honolulu, HI 96822, USA
- ⁶¹ Dipartimento di Fisica e Astronomia "Augusto Righi" - Alma Mater Studiorum Università di Bologna, Viale Berti Pichat 6/2, 40127 Bologna, Italy
- ⁶² Instituto de Astrofísica de Canarias, Vía Láctea, 38205 La Laguna, Tenerife, Spain
- ⁶³ Institute for Astronomy, University of Edinburgh, Royal Observatory, Blackford Hill, Edinburgh EH9 3HJ, UK
- ⁶⁴ Jodrell Bank Centre for Astrophysics, Department of Physics and Astronomy, University of Manchester, Oxford Road, Manchester M13 9PL, UK
- ⁶⁵ European Space Agency/ESRIN, Largo Galileo Galilei 1, 00044 Frascati, Roma, Italy
- ⁶⁶ Université Claude Bernard Lyon 1, CNRS/IN2P3, IP2I Lyon, UMR 5822, Villeurbanne, F-69100, France
- ⁶⁷ Institut de Ciències del Cosmos (ICCUB), Universitat de Barcelona (IEEC-UB), Martí i Franquès 1, 08028 Barcelona, Spain
- ⁶⁸ Institució Catalana de Recerca i Estudis Avançats (ICREA), Passeig de Lluís Companys 23, 08010 Barcelona, Spain
- ⁶⁹ UCB Lyon 1, CNRS/IN2P3, IUF, IP2I Lyon, 4 rue Enrico Fermi, 69622 Villeurbanne, France
- ⁷⁰ Mullard Space Science Laboratory, University College London, Holmbury St Mary, Dorking, Surrey RH5 6NT, UK
- ⁷¹ Departamento de Física, Faculdade de Ciências, Universidade de Lisboa, Edifício C8, Campo Grande, PT1749-016 Lisboa, Portugal
- ⁷² Instituto de Astrofísica e Ciências do Espaço, Faculdade de Ciências, Universidade de Lisboa, Campo Grande, 1749-016 Lisboa, Portugal

- 73 INFN-Padova, Via Marzolo 8, 35131 Padova, Italy
- 74 Aix-Marseille Université, CNRS/IN2P3, CPPM, Marseille, France
- 75 INFN-Bologna, Via Imerio 46, 40126 Bologna, Italy
- 76 FRACTAL S.L.N.E., calle Tulipán 2, Portal 13 1A, 28231, Las Rozas de Madrid, Spain
- 77 NRC Herzberg, 5071 West Saanich Rd, Victoria, BC V9E 2E7, Canada
- 78 Institute of Theoretical Astrophysics, University of Oslo, P.O. Box 1029 Blindern, 0315 Oslo, Norway
- 79 Jet Propulsion Laboratory, California Institute of Technology, 4800 Oak Grove Drive, Pasadena, CA, 91109, USA
- 80 Department of Physics, Lancaster University, Lancaster, LA1 4YB, UK
- 81 Felix Hormuth Engineering, Goethestr. 17, 69181 Leimen, Germany
- 82 Technical University of Denmark, Elektrovej 327, 2800 Kgs. Lyngby, Denmark
- 83 Cosmic Dawn Center (DAWN), Denmark
- 84 Institut d'Astrophysique de Paris, UMR 7095, CNRS, and Sorbonne Université, 98 bis boulevard Arago, 75014 Paris, France
- 85 NASA Goddard Space Flight Center, Greenbelt, MD 20771, USA
- 86 Department of Physics and Helsinki Institute of Physics, Gustaf Hällströmin katu 2, 00014 University of Helsinki, Finland
- 87 Université de Genève, Département de Physique Théorique and Centre for Astroparticle Physics, 24 quai Ernest-Ansermet, CH-1211 Genève 4, Switzerland
- 88 Department of Physics, P.O. Box 64, 00014 University of Helsinki, Finland
- 89 Helsinki Institute of Physics, Gustaf Hällströmin katu 2, University of Helsinki, Helsinki, Finland
- 90 Centre de Calcul de l'IN2P3/CNRS, 21 avenue Pierre de Coubertin 69627 Villeurbanne Cedex, France
- 91 Laboratoire d'étude de l'Univers et des phénomènes eXtremes, Observatoire de Paris, Université PSL, Sorbonne Université, CNRS, 92190 Meudon, France
- 92 Aix-Marseille Université, CNRS, CNES, LAM, Marseille, France
- 93 SKA Observatory, Jodrell Bank, Lower Withington, Macclesfield, Cheshire SK11 9FT, UK
- 94 Dipartimento di Fisica "Aldo Pontremoli", Università degli Studi di Milano, Via Celoria 16, 20133 Milano, Italy
- 95 INFN-Sezione di Milano, Via Celoria 16, 20133 Milano, Italy
- 96 University of Applied Sciences and Arts of Northwestern Switzerland, School of Computer Science, 5210 Windisch, Switzerland
- 97 Universität Bonn, Argelander-Institut für Astronomie, Auf dem Hügel 71, 53121 Bonn, Germany
- 98 INFN-Sezione di Roma, Piazzale Aldo Moro, 2 - c/o Dipartimento di Fisica, Edificio G. Marconi, 00185 Roma, Italy
- 99 Department of Physics, Institute for Computational Cosmology, Durham University, South Road, Durham, DH1 3LE, UK
- 100 Université Côte d'Azur, Observatoire de la Côte d'Azur, CNRS, Laboratoire Lagrange, Bd de l'Observatoire, CS 34229, 06304 Nice cedex 4, France
- 101 Université Paris Cité, CNRS, Astroparticule et Cosmologie, 75013 Paris, France
- 102 CNRS-UCB International Research Laboratory, Centre Pierre Binetruy, IRL2007, CPB-IN2P3, Berkeley, USA
- 103 University of Applied Sciences and Arts of Northwestern Switzerland, School of Engineering, 5210 Windisch, Switzerland
- 104 Institut d'Astrophysique de Paris, 98bis Boulevard Arago, 75014, Paris, France
- 105 Institute of Physics, Laboratory of Astrophysics, Ecole Polytechnique Fédérale de Lausanne (EPFL), Observatoire de Sauverny, 1290 Versoix, Switzerland
- 106 Aurora Technology for European Space Agency (ESA), Camino bajo del Castillo, s/n, Urbanización Villafranca del Castillo, Villanueva de la Cañada, 28692 Madrid, Spain
- 107 Institut de Física d'Altes Energies (IFAE), The Barcelona Institute of Science and Technology, Campus UAB, 08193 Bellaterra (Barcelona), Spain
- 108 School of Mathematics, Statistics and Physics, Newcastle University, Herschel Building, Newcastle-upon-Tyne, NE1 7RU, UK
- 109 DARK, Niels Bohr Institute, University of Copenhagen, Jagtvej 155, 2200 Copenhagen, Denmark
- 110 Waterloo Centre for Astrophysics, University of Waterloo, Waterloo, Ontario N2L 3G1, Canada
- 111 Department of Physics and Astronomy, University of Waterloo, Waterloo, Ontario N2L 3G1, Canada
- 112 Perimeter Institute for Theoretical Physics, Waterloo, Ontario N2L 2Y5, Canada
- 113 Institute of Space Science, Str. Atomistilor, nr. 409 Măgurele, Ilfov, 077125, Romania
- 114 Consejo Superior de Investigaciones Científicas, Calle Serrano 117, 28006 Madrid, Spain
- 115 Universidad de La Laguna, Departamento de Astrofísica, 38206 La Laguna, Tenerife, Spain
- 116 Caltech/IPAC, 1200 E. California Blvd., Pasadena, CA 91125, USA
- 117 Institut für Theoretische Physik, University of Heidelberg, Philosophenweg 16, 69120 Heidelberg, Germany
- 118 Institut de Recherche en Astrophysique et Planétologie (IRAP), Université de Toulouse, CNRS, UPS, CNES, 14 Av. Edouard Belin, 31400 Toulouse, France
- 119 Université St Joseph; Faculty of Sciences, Beirut, Lebanon
- 120 Departamento de Física, FCFM, Universidad de Chile, Blanco Encalada 2008, Santiago, Chile
- 121 Universität Innsbruck, Institut für Astro- und Teilchenphysik, Technikerstr. 25/8, 6020 Innsbruck, Austria
- 122 Satlantís, University Science Park, Sede Bld 48940, Leioa-Bilbao, Spain
- 123 Infrared Processing and Analysis Center, California Institute of Technology, Pasadena, CA 91125, USA
- 124 Instituto de Astrofísica e Ciências do Espaço, Faculdade de Ciências, Universidade de Lisboa, Tapada da Ajuda, 1349-018 Lisboa, Portugal
- 125 Cosmic Dawn Center (DAWN)
- 126 Niels Bohr Institute, University of Copenhagen, Jagtvej 128, 2200 Copenhagen, Denmark
- 127 Universidad Politécnica de Cartagena, Departamento de Electrónica y Tecnología de Computadoras, Plaza del Hospital 1, 30202 Cartagena, Spain
- 128 Dipartimento di Fisica e Scienze della Terra, Università degli Studi di Ferrara, Via Giuseppe Saragat 1, 44122 Ferrara, Italy
- 129 Istituto Nazionale di Fisica Nucleare, Sezione di Ferrara, Via Giuseppe Saragat 1, 44122 Ferrara, Italy
- 130 Department of Physics, Oxford University, Keble Road, Oxford OX1 3RH, UK
- 131 Université PSL, Observatoire de Paris, Sorbonne Université, CNRS, LERMA, 75014, Paris, France
- 132 Université Paris-Cité, 5 Rue Thomas Mann, 75013, Paris, France
- 133 Zentrum für Astronomie, Universität Heidelberg, Philosophenweg 12, 69120 Heidelberg, Germany
- 134 INAF-Osservatorio Astronomico di Brera, Via Brera 28, 20122 Milano, Italy, and INFN-Sezione di Genova, Via Dodecaneso 33, 16146, Genova, Italy
- 135 ICL, Junia, Université Catholique de Lille, LITL, 59000 Lille, France
- 136 ICSC - Centro Nazionale di Ricerca in High Performance Computing, Big Data e Quantum Computing, Via Magnanelli 2, Bologna, Italy
- 137 Instituto de Física Teórica UAM-CSIC, Campus de Cantoblanco, 28049 Madrid, Spain
- 138 CERCA/ISO, Department of Physics, Case Western Reserve University, 10900 Euclid Avenue, Cleveland, OH 44106, USA
- 139 Technical University of Munich, TUM School of Natural Sciences, Physics Department, James-Franck-Str. 1, 85748 Garching, Germany
- 140 Max-Planck-Institut für Astrophysik, Karl-Schwarzschild-Str. 1, 85748 Garching, Germany

- ¹⁴¹ Laboratoire Univers et Théorie, Observatoire de Paris, Université PSL, Université Paris Cité, CNRS, 92190 Meudon, France
- ¹⁴² Departamento de Física Fundamental. Universidad de Salamanca. Plaza de la Merced s/n. 37008 Salamanca, Spain
- ¹⁴³ Université de Strasbourg, CNRS, Observatoire astronomique de Strasbourg, UMR 7550, 67000 Strasbourg, France
- ¹⁴⁴ Center for Data-Driven Discovery, Kavli IPMU (WPI), UTIAS, The University of Tokyo, Kashiwa, Chiba 277-8583, Japan
- ¹⁴⁵ California Institute of Technology, 1200 E California Blvd, Pasadena, CA 91125, USA
- ¹⁴⁶ Department of Physics & Astronomy, University of California Irvine, Irvine CA 92697, USA
- ¹⁴⁷ Department of Mathematics and Physics E. De Giorgi, University of Salento, Via per Arnesano, CP-193, 73100, Lecce, Italy
- ¹⁴⁸ INFN, Sezione di Lecce, Via per Arnesano, CP-193, 73100, Lecce, Italy
- ¹⁴⁹ INAF-Sezione di Lecce, c/o Dipartimento Matematica e Fisica, Via per Arnesano, 73100, Lecce, Italy
- ¹⁵⁰ Departamento Física Aplicada, Universidad Politécnica de Cartagena, Campus Muralla del Mar, 30202 Cartagena, Murcia, Spain
- ¹⁵¹ Instituto de Física de Cantabria, Edificio Juan Jordá, Avenida de los Castros, 39005 Santander, Spain
- ¹⁵² CEA Saclay, DFR/IRFU, Service d'Astrophysique, Bat. 709, 91191 Gif-sur-Yvette, France
- ¹⁵³ Department of Computer Science, Aalto University, PO Box 15400, Espoo, FI-00 076, Finland
- ¹⁵⁴ Instituto de Astrofísica de Canarias, c/ Via Lactea s/n, La Laguna 38200, Spain. Departamento de Astrofísica de la Universidad de La Laguna, Avda. Francisco Sanchez, La Laguna, 38200, Spain
- ¹⁵⁵ Ruhr University Bochum, Faculty of Physics and Astronomy, Astronomical Institute (AIRUB), German Centre for Cosmological Lensing (GCCL), 44780 Bochum, Germany
- ¹⁵⁶ Department of Physics and Astronomy, Vesilinnantie 5, 20014 University of Turku, Finland
- ¹⁵⁷ Serco for European Space Agency (ESA), Camino bajo del Castillo, s/n, Urbanizacion Villafranca del Castillo, Villanueva de la Cañada, 28692 Madrid, Spain
- ¹⁵⁸ ARC Centre of Excellence for Dark Matter Particle Physics, Melbourne, Australia
- ¹⁵⁹ Centre for Astrophysics & Supercomputing, Swinburne University of Technology, Hawthorn, Victoria 3122, Australia
- ¹⁶⁰ Department of Physics and Astronomy, University of the Western Cape, Bellville, Cape Town, 7535, South Africa
- ¹⁶¹ DAMTP, Centre for Mathematical Sciences, Wilberforce Road, Cambridge CB3 0WA, UK
- ¹⁶² Kavli Institute for Cosmology Cambridge, Madingley Road, Cambridge, CB3 0HA, UK
- ¹⁶³ Department of Astrophysics, University of Zurich, Winterthurerstrasse 190, 8057 Zurich, Switzerland
- ¹⁶⁴ Department of Physics, Centre for Extragalactic Astronomy, Durham University, South Road, Durham, DH1 3LE, UK
- ¹⁶⁵ IRFU, CEA, Université Paris-Saclay 91191 Gif-sur-Yvette Cedex, France
- ¹⁶⁶ Oskar Klein Centre for Cosmoparticle Physics, Department of Physics, Stockholm University, Stockholm, SE-106 91, Sweden
- ¹⁶⁷ Astrophysics Group, Blackett Laboratory, Imperial College London, London SW7 2AZ, UK
- ¹⁶⁸ Univ. Grenoble Alpes, CNRS, Grenoble INP, LPSC-IN2P3, 53, Avenue des Martyrs, 38000, Grenoble, France
- ¹⁶⁹ Dipartimento di Fisica, Sapienza Università di Roma, Piazzale Aldo Moro 2, 00185 Roma, Italy
- ¹⁷⁰ Centro de Astrofísica da Universidade do Porto, Rua das Estrelas, 4150-762 Porto, Portugal
- ¹⁷¹ HE Space for European Space Agency (ESA), Camino bajo del Castillo, s/n, Urbanizacion Villafranca del Castillo, Villanueva de la Cañada, 28692 Madrid, Spain
- ¹⁷² Dipartimento di Fisica - Sezione di Astronomia, Università di Trieste, Via Tiepolo 11, 34131 Trieste, Italy
- ¹⁷³ Department of Astrophysical Sciences, Peyton Hall, Princeton University, Princeton, NJ 08544, USA
- ¹⁷⁴ Theoretical astrophysics, Department of Physics and Astronomy, Uppsala University, Box 515, 751 20 Uppsala, Sweden
- ¹⁷⁵ Minnesota Institute for Astrophysics, University of Minnesota, 116 Church St SE, Minneapolis, MN 55455, USA
- ¹⁷⁶ Mathematical Institute, University of Leiden, Einsteinweg 55, 2333 CA Leiden, The Netherlands
- ¹⁷⁷ ASTRON, the Netherlands Institute for Radio Astronomy, Postbus 2, 7990 AA, Dwingeloo, The Netherlands
- ¹⁷⁸ Center for Advanced Interdisciplinary Research, Ss. Cyril and Methodius University in Skopje, Macedonia
- ¹⁷⁹ Institute of Astronomy, University of Cambridge, Madingley Road, Cambridge CB3 0HA, UK
- ¹⁸⁰ Space physics and astronomy research unit, University of Oulu, Pentti Kaiteran katu 1, FI-90014 Oulu, Finland
- ¹⁸¹ Center for Computational Astrophysics, Flatiron Institute, 162 5th Avenue, 10010, New York, NY, USA
- ¹⁸² Department of Astronomy, University of Massachusetts, Amherst, MA 01003, USA
- ¹⁸³ Department of Physics and Astronomy, University of British Columbia, Vancouver, BC V6T 1Z1, Canada

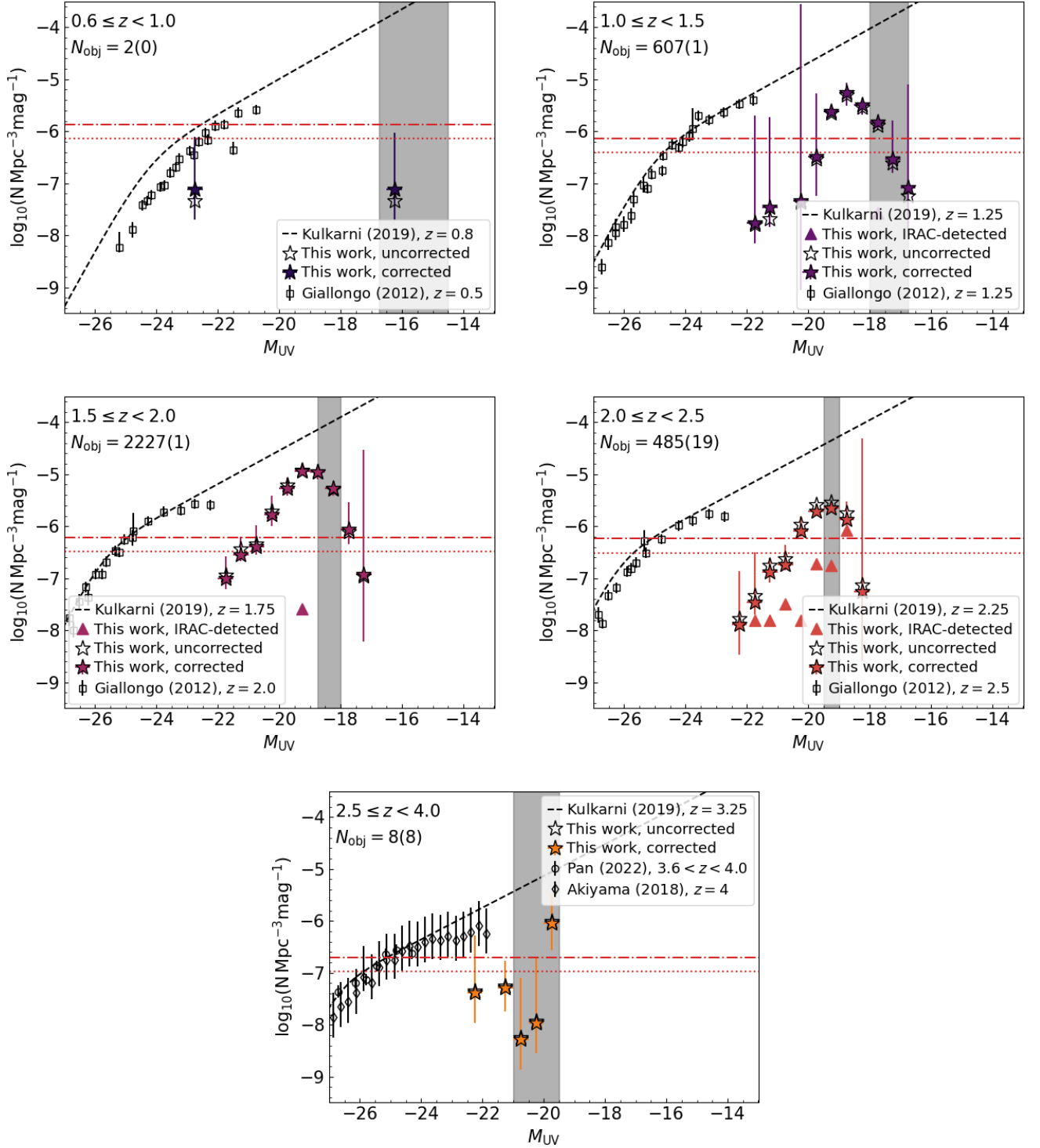


Fig. 9. UV luminosity function of the LRD candidates from $z = 0$ (top left) to $z = 4$ (bottom right). Empty stars indicate the values before any corrections, while the coloured stars show the density after correcting for completeness and redshift estimation. Coloured triangles show the conservative estimation derived considering only IRAC-detected sources. The black vertical shaded regions show the range of the 80% completeness in the three fields. In the top left we report the number of objects inside the redshift bin and, in brackets, the number of IRAC-detected sources in the bin. Empty symbols show UV luminosity functions of QSOs from Giallongo et al. (2012), and reference therein, Akiyama et al. (2018), and Pan et al. (2022). We also report the UV luminosity function of QSOs modelled by Kulkarni et al. (2019, black dashed line). For a comparison, the red horizontal dash-dotted line shows the minimum density probed by HST CANDELS survey (0.29 deg^2 Grogin et al. 2011), while the red horizontal dotted line shows the minimum density probed by the JWST COSMOS-WEB survey (0.54 deg^2 Casey et al. 2023).

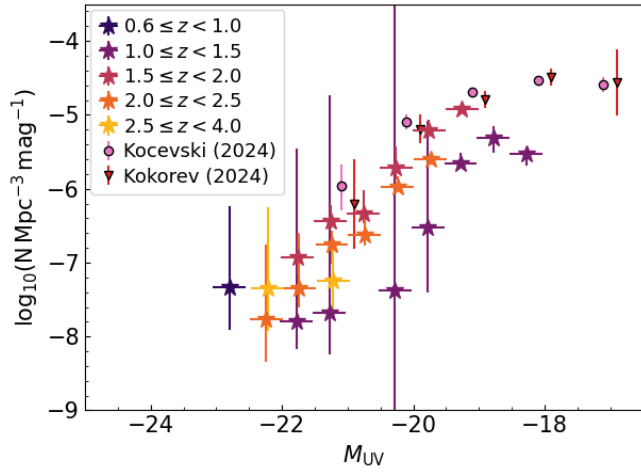


Fig. 10. Comparison of the corrected UV luminosity function of LRD candidates derived in this work from $z = 0$ to $z = 4$, as well as values at $z = 6$ from the literature (Kocevski et al. 2024; Kokorev et al. 2024a).

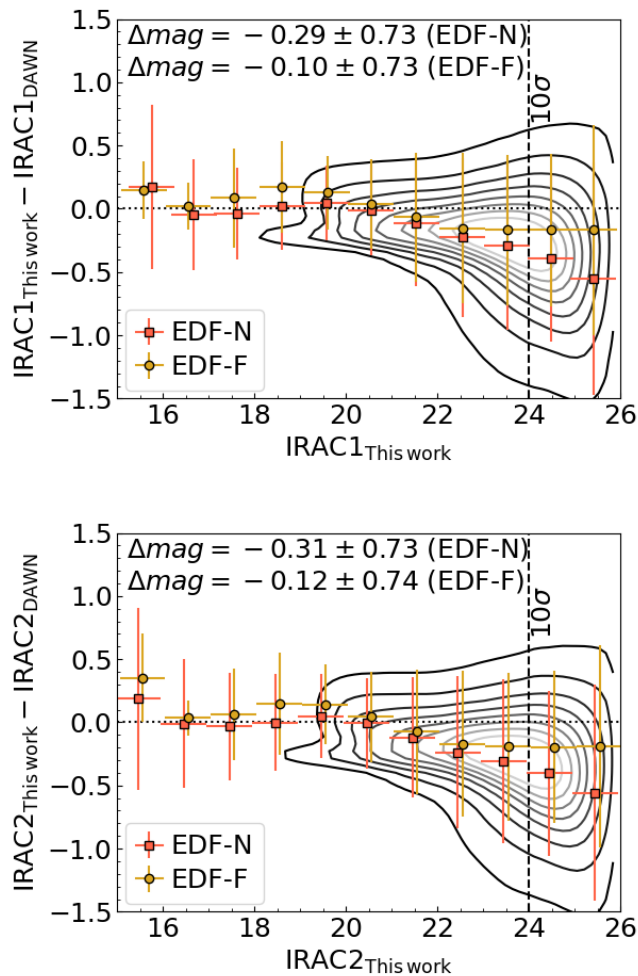


Fig. A.1. Difference between the magnitudes derived in this work and the ones in the Cosmic Dawn Catalogue. The black contours show the distribution of all sources in common between the two catalogues (from 10% to 90% of the sample), while red squares and yellow circles show the average values in magnitude bins for the EDF-N and EDF-F, respectively. We report in the top left the mean and standard deviation of the difference in magnitude in the two fields. We report results for the IRAC1 filter on the top and the IRAC2 filter on the bottom panel.

Appendix A: IRAC photometry comparison

In this Section we show the comparison between the IRAC photometry derived in this work (see Sect. 2.2) and the one from the Cosmic Dawn Survey Catalogue (Euclid Collaboration: Zalesky et al. 2024). This comparison is possible only in the EDF-N and EDF-F, as the Cosmic Dawn Catalogues are not available for the EDF-S. Sources are matched considering a $1''$ radius, but we verify that the difference does not change significantly considering a smaller matching radius.

As visible in Fig. A.1, the magnitude estimated in our work are, on average, slightly underestimated by -0.10 magnitudes in the EDF-F and -0.30 magnitudes in the EDF-N. These differences are mainly dominated by faint sources as they decrease to $\Delta\text{IRAC1} = 0.07 \pm 0.34$ and $\Delta\text{IRAC2} = 0.07 \pm 0.35$ in the EDF-F and $\Delta\text{IRAC1} = 0.01 \pm 0.34$ and $\Delta\text{IRAC2} = 0.01 \pm 0.35$ in the EDF-N when we limit the analysis to sources brighter than 21 in the respective bands.

Appendix B: Redshift recovery

The *Euclid* pipeline, at the moment, lacks LRD templates. This can have a direct impact on the redshift estimation for these objects. We therefore decided to test the redshift recovery for LRDs by simulating *Euclid* observations of LRDs and input this mock photometry to the *Euclid* pipeline.

In particular, we start by simulating simple LRD spectra, using two power laws, with red and blue continuum slopes at rest-frame optical and UV wavelengths. For the β_{UV} and β_{opt} continuum slopes, we considered the values measured by Kocevski et al. (2024) for a sample of 341 LRDs at $z = 2-11$, but with a median redshift of $z = 6.4$. We used these mock LRDs as templates, moving them from $z = 1$ to $z = 7.6$, where we have enough bands to measure the two slopes in all EDFs. We scale their absolute UV magnitudes (M_{UV}) and compare these with the *Euclid* observational depths. We then derive photometric redshift, considering the same setup used in the *Euclid* pipeline.

In the top panel of Fig. B.1 we report the comparison between the recovered and input redshifts. As can be seen, the first effect is a bimodal distribution, with some galaxies that are wrongly placed at $z < 2$. In addition, the output redshift tends to be overestimated for galaxies at $z_{\text{input}} < 2$, while the upper limit at $z = 6$ naturally underestimate the redshift of $z > 6$ sources. Overall, we have around 40% of outliers (f_{out}), defined as galaxies with $|\delta z| = |z_{\text{output}} - z_{\text{input}}| / (1 + z_{\text{input}}) > 0.15$. If we remove these outliers, we obtain a distribution consistent with no redshift bias, since $\delta z = 0.02 \pm 0.07$.

In the bottom panel of Fig. B.1 we instead show the comparison between the true redshift and the one recovered by fitting the mock photometry with a double power law and leaving the redshift free to vary (see Sect. 3). In this fit, we considered the pipeline redshift as a starting point and the uncertainties as limits. We verified that leaving the redshift totally free improves the results. This refinement in the redshift produces a substantial reduction in the outlier fraction, more than halving it ($f_{\text{out}} = 12\%$). At the same time, the biases at the different redshifts are similar and the $z = 6$ upper limit is removed. The expected mean redshift bias, after removing the outliers, is also slightly improved, becoming $\delta z = 0.01 \pm 0.05$.

By comparing the intrinsic redshift distribution and the one derived after the two power-law fit, we derived an average redshift correction to apply to the estimated luminosity function (Sect. 4.4). These redshift corrections are derived in redshift bins and are: 0.60 at $z = 1.0-1.5$; 0.91 at $z = 1.5-2.0$; 1.32 at $z = 2.0-2.5$; 1.09 at $z = 2.5-4.0$; and 1.09 at $z = 4.0-6.0$

Appendix C: Impact of slope uncertainties on sample selection

In this Section we focus on the impact of the uncertainties of the rest-frame UV and optical slopes on the sample selection. In particular, we start from the subsamples of sources with $S/N > 3$ in more than four filters. We then randomise the rest-frame UV and optical slopes 100 times, using a normal distribution centred on the best value and with standard deviation equal to the respective uncertainties. After this randomization, we select for each iteration the number of v-shape sources, checking then the subsample of these objects that is also compact, is not contaminated by nebular emission lines and has a $\chi^2 < 100$. We do not perform the visual check of all sources selected in the different iterations.

In Table C.1 we report the 16% and 84% of the distribution of the number of selected objects in the different fields. As visible,

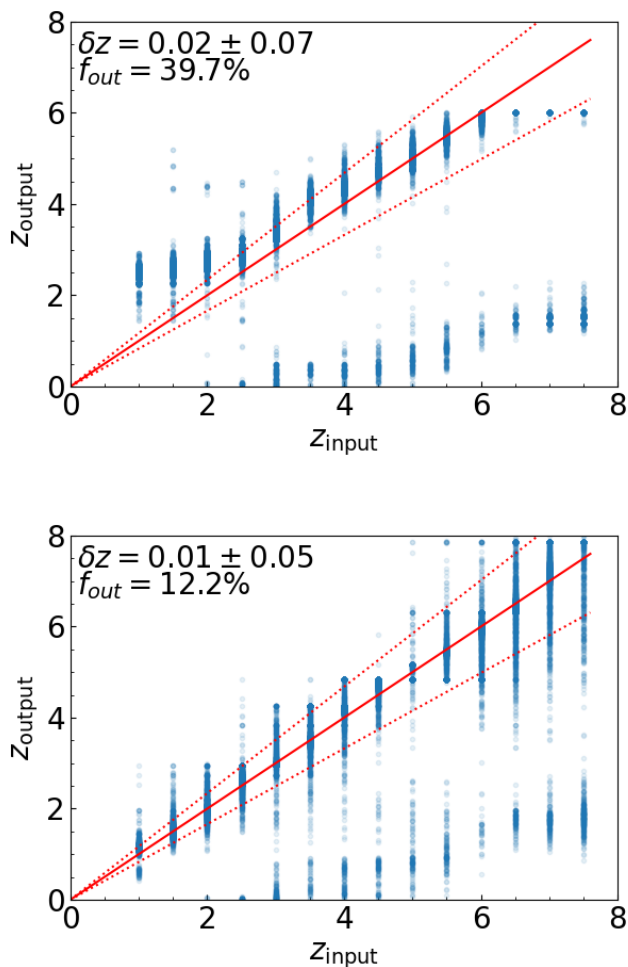


Fig. B.1. Redshift recovery using the *Euclid* pipeline (top) and with the double power-law fit improvement (bottom). In the upper right of each panel we report the fraction of outliers, defined as objects with $|\delta z| = |z_{\text{output}} - z_{\text{input}}| / (1 + z_{\text{input}}) > 0.15$, as well as the mean and standard deviation of δz , measured after removing the outliers.

the values are larger than the one reported in Table 3, indicating that the number of LRD candidates may be underestimated due to the uncertainties on the rest-frame UV and optical slopes. However, given that the number of potential contaminants is expected to be larger than the number of LRD, we prefer to keep the conservative estimates derived in the main text of this work.

Appendix D: Complete sample

In Table D.1 we include the final list of LRD candidates and their properties, derived using the double power law fit described in Sect. 3 and whose performance is shown with mock data in Appendix B.

Table C.1. 16% and 84% percentages of the number of selected objects when randomising the slope measurements.

	EDF-F	EDF-N IRAC	EDF-S	EDF-F	EDF-N No-IRAC, $z \leq 2.1$	EDF-S
v-shape continuum	(3700, 3824)	(1997, 2071)	(12 625 12 839)	(112 290, 112 823)	(106 490, 106 997)	(226 002, 226 804)
Compact	(228, 253)	(100, 120)	(670, 716)	(3439, 3533)	(3092, 3189)	(7010, 7144)
No emission lines	(163, 190)	(49, 62)	(378, 414)	(2845, 2936)	(2375, 2451)	(5764, 5890)
$\chi^2 < 100$	(151, 170)	(38, 49)	(357, 391)	(2806, 2900)	(2211, 2287)	(5674, 5798)

Table D.1. Properties of LRD candidates.

ID	RA [deg]	Dec [deg]	z	σ_z	M_{UV}	$\sigma_{M_{UV}}$	β_{UV}	$\sigma_{\beta_{UV}}$	β_{opt}	$\sigma_{\beta_{opt}}$
-508115529279019500	50.811552941129854	-27.9019500031698870	1.73	0.04	-19.3	0.4	-2.5	0.8	1.3	0.7
-509746984272137369	50.974698421974345	-27.2137369299800260	1.43	0.01	-19.1	0.4	-2.3	0.6	0.4	0.4
-506780226277952382	50.678022675402380	-27.7952382847731400	1.84	0.09	-19.2	0.2	-2.0	0.5	1.0	0.5
-508524594269841903	50.852459401007260	-26.9841903597850700	2.08	0.05	-19.4	0.2	-1.2	0.5	0.2	0.7
-508984186271393227	50.898418618770854	-27.1393227401735600	2.04	0.01	-19.1	0.4	-1.3	0.7	0.8	0.9
-509604641270953419	50.960464128672700	-27.0953419499146230	1.56	0.07	-18.5	0.5	-1.7	0.8	0.8	0.5
-508222098269760365	50.822209897801020	-26.9760365959727970	1.93	0.02	-19.6	0.2	-1.5	0.4	0.2	0.5
-508762123270516640	50.876212385949394	-27.0516640856371570	1.56	0.01	-19.4	0.3	-2.6	0.6	0.1	0.5
-508397504271496709	50.839750412997640	-27.1496709862933120	2.04	0.07	-19.1	0.4	-1.8	0.9	1.4	1.2
-509723625268249072	50.972362526891885	-26.8249072402469050	1.67	0.19	-18.4	0.5	-1.3	0.6	0.4	0.6

Notes. Here we report the first 10 objects, while the complete list is available online.